Airway Closure: Surface-tension-driven non-axisymmetric instabilities of liquid-lined elastic rings

Matthias Heil* and Joseph P. White
Department of Mathematics
University of Manchester
Oxford Road
Manchester M13 9PL, U.K.

December 20, 2001

Journal of Fluid Mechanics (in print)

Abstract

This paper investigates the stability and large-displacement post-buckling behaviour of liquid-lined elastic rings. The fluid flow and the wall deformation are described by the free-surface Navier-Stokes equations and by geometrically non-linear shell theory, respectively. The fluid-structure interaction problem is solved numerically by a finite element method. The compressive load on the ring is a combination of the external pressure and the effect of surface-tension. Once this combined load exceeds a critical value, the subsequent non-axisymmetric collapse of the ring is controlled by the dynamics of the surface-tension-driven redistribution of fluid in the liquid lining. It is shown that, for sufficiently large surface tension, the ring can undergo a catastrophic collapse which leads to a complete occlusion of its lumen. A novel lubrication theory model, which ensures exact volume conservation for flows on strongly curved substrates, is developed and found to be capable of accurately describing the motion of the air-liquid interface and the fluid-structure interaction in the large-displacement regime, even in cases where the film thickness is large.

The findings have important implications for the occurrence of airway closure in lung diseases (such as oedema) which cause an increase in the thickness of the airways' liquid lining. It is shown that under such conditions, airways can become occluded even if the volume of fluid in their liquid lining is much smaller than that required to occlude them in their axisymmetric state.

1 Introduction

The airways of the lung are thin-walled elastic vessels which are lined with a thin liquid film. This liquid film can undergo a surface-tension-driven fluid-elastic instability which may lead to airway closure via the formation of an occluding liquid bridge (Halpern & Grotberg 1992). Airway closure in the small airways tends to occur towards the end of expiration when the airway diameters are smallest (Hughes

*Author to whom correspondence should be addressed.

et al. 1970). In healthy adults, the occluding liquid bridges rupture during the early stages of inspiration and do not interfere significantly with gas exchange (West 1985, Forgacs 1978, Widdicombe & Davies 1991; see, e.g., Howell *et al.* 2000 for a model of airway reopening via liquid bridge rupture and Gaver *et al.* (1996) for a model of the reopening of strongly collapsed airways). However, in a variety of diseases, such as emphysema and cystic fibrosis, airway closure can occur in the larger airways and persists for a much larger fraction of the breathing cycle. In extreme cases, the airway can remain completely occluded. This problem is particularly common in prematurely born infants whose lungs have not yet begun to produce the surfactant that reduces the surface tension of the liquid lining to normal levels. The elevated surface tension makes their airways strongly liable to collapse and causes severe breathing difficulties. This condition is known as neonatal Respiratory Distress Syndrome and is responsible for a large number of infant deaths. It is important to understand the mechanisms leading to airway closure in order to improve the treatment of such diseases.

Airway closure is initiated by the classical axisymmetric Rayleigh instability: the liquid film inside a rigid cylindrical tube whose length exceeds its circumference is unstable to axisymmetric perturbations which cause fluid to drain into axisymmetric lobes (Rayleigh, 1902). If the volume of fluid in the liquid lining is sufficiently large, the non-linear growth of the instability can reduce the minimum radius of the axisymmetric air-liquid interface to zero and thus lead to the formation of an axisymmetric occluding liquid bridge (see, e.g. Johnson *et al.* 1991, Everett & Haynes 1972). If the volume of fluid is small, the air-liquid interface evolves towards an unduloidal shape and the tube remains open.

The small radius of the distal airways and bronchioli results in considerable surface-tension-induced pressure jumps over the highly curved air-liquid interfaces. These can be large enough to induce large deformations of the airway walls. Halpern & Grotberg (1992) showed that wall elasticity significantly reduces the minimum volume of fluid required to form an occluding liquid bridge in an airway because the reduced fluid pressure in the growing lobes pulls the airway walls radially inwards. This reduces the minimum radius of the air-liquid interface and thus facilitates the formation of an occluding liquid bridge.

Halpern & Grotberg's (1992) study was restricted to axisymmetric deformations and their results showed that, for parameter values which are representative of the condition in the small airways, the surface-tension-induced axisymmetric wall deformations can be quite large (up to 10% of the tube's undeformed radius). Motivated by the observation that thin-walled cylindrical tubes tend to buckle non-axisymmetrically when subjected to such strong compression, Heil (1999*a*) and Heil (1999*b*) investigated the static stability of elastic cylindrical tubes, occluded by axisymmetric liquid bridges. He showed that, for Halpern & Grotberg's (1992) parameter values, the axisymmetric state is statically unstable to non-axisymmetric perturbations. This implies that, once an axisymmetric liquid bridge has been formed, the airway wall will buckle strongly, redistributing the fluid contained in the liquid bridge over a large axial distance.

Heil's (1999*b*) study also showed that in non-axisymmetrically buckled tubes, occluding liquid bridges can be formed with a fraction of the fluid volume required to occlude a corresponding axisymmetric tube. In the context of the airway closure problem, however, the mere *existence* of such non-axisymmetric occluding liquid bridges of small volume does not guarantee that they can be realised in the course of the system's evolution from the initially uniform axisymmetric state. If the tube wall does not buckle until an axisymmetric liquid bridge is formed, then airway closure at smaller fluid volumes remains impossible. This observation forms the motivation for the current study. We aim to determine if liquid-lined elastic tubes that do not contain enough fluid to form an axisymmetric occluding liquid bridge can undergo a non-axisymmetric instability that leads to airway closure. Ultimately, this question must be addressed by studying the time-dependent stability of the evolving axisymmetric system (undergoing Halpern & Grotberg's 1992 primary instability) to non-axisymmetric perturbations. In the present paper, we consider a simplified 2D model problem in which a liquid-lined elastic ring is subject to an external pressure p^*_{ext} (representing the pleural pressure acting on the airway) and to the additional compression due to the surface tension at the air-liquid interface. We wish to investigate the time-dependent behaviour of this system once p^*_{ext} has exceeded the buckling pressure $p^{*(buckl)}_{ext}$. The value of $p^{*(buckl)}_{ext}$ follows from the static stability analyses of Hill *et al.* (1997) and Rosenzweig & Jensen (2001). These studies also provide an overview of the system's multiple non-axisymmetric equilibrium configurations which represent the possible asymptotic states towards which the system can evolve after the loss of stability. A time-dependent analysis is required to determine **(i)** which of these equilibrium states are realisable via a continuous evolution from the axisymmetric pre-buckling state and **(ii)** the time-scale over which this evolution takes place.

Since the two-dimensional model considered in this study neglects any axial variations, it is important to assess beforehand how any results might be affected by three-dimensional effects in the airways of the lung. We believe that a three-dimensional tube, lined with a liquid film of a given thickness, will always be more unstable than the corresponding ring. This assumption is based on the following argument: a ring, lined with a constant volume of fluid, can only become unstable to non-axisymmetric perturbations if the external pressure is raised above the buckling pressure. In a three-dimensional tube, the axisymmetric redistribution of fluid caused by the Rayleigh instability results in a significant increase in the film thickness and hence in an increase in the tube's compression in the regions where the axisymmetric lobes are being formed. This additional, local compression can become strong enough to cause the axisymmetric state to lose its stability. Therefore, any parameter combinations for which airway closure is predicted in the two-dimensional system can also be expected result in airway closure in the corresponding three-dimensional system.

The outline of the paper is as follows: section 2 provides a detailed description of the model problem and introduces the wall model and the two fluid models (the Navier-Stokes equations and a volume-conserving lubrication theory model) used to represent the flow in the liquid lining. The numerical technique employed to solve the coupled fluid-structure interaction problem is discussed next. Section 3 presents the results of the computations and investigates the accuracy of the volume-conserving lubrication theory model. The success of this simple model provides insight into the fluid mechanics in this problem. Finally, section 4 discusses the relevance of the results for the airway closure problem.

2 The model

We consider the following model problem: a uniform elastic ring of wall thickness h, undeformed radius R_0 and density ρ_w is lined with a viscous fluid of viscosity μ, density ρ and surface tension σ^*. The volume of fluid in the liquid lining is such that it forms a film of uniform non-dimensional thickness $H_0 = H_0^*/R_0$ when the ring is undeformed; throughout this paper superscript stars will be used to distinguish dimensional quantities from their non-dimensional equivalents. The ring is subject to an external pressure p^*_{ext} relative to the air pressure in the lumen which we arbitrarily set to zero.

2.1 The wall equations

We use geometrically non-linear shell theory to describe the deformation of the thin-walled elastic ring in response to the load $\mathbf{f}^*$ exerted on it by the liquid lining and the external pressure. For this purpose we parametrise the non-dimensional position vector to material particles in the undeformed configuration, $\mathbf{r}_w = \mathbf{r}^*_w/R_0$, by the non-dimensional Lagrangian coordinate $\zeta = \zeta^*/R_0$, measured along the ring's centreline such that $\mathbf{r}_w(\zeta) = (\cos(\zeta), \sin(\zeta))$. When the ring deforms, material points are displaced by the vector $\mathbf{v}(\zeta)$ such that their new position becomes $\mathbf{R}_w(\zeta) = \mathbf{r}_w(\zeta) + \mathbf{v}(\zeta)$. We decompose the displacement vector into its tangential and radial components (relative to the reference configuration), i.e. $\mathbf{v} = v^1\mathbf{t}_w + v^2\mathbf{n}_w$; see Fig. 1(a).

Buckling of thin-walled rings typically involves large transverse deflections which are accompanied by small extensional deformations. Therefore, we assume that the relation between stress and strain is given by the plane strain Hooke's law. Under these conditions, the principle of virtual displacements which governs the ring's deformation is given by

$$\int_0^{2\pi} \left[\gamma\ \delta\gamma + \frac{1}{12}\left(\frac{h}{R_0}\right)^2 \kappa\ \delta\kappa - \frac{1}{12}\left(\frac{h}{R_0}\right)^3 \left(\left(\frac{R_0}{h}\right)\mathbf{f} - \lambda_T^2\ \frac{\partial^2 \mathbf{R}_w}{\partial t^2}\right)\cdot \delta\mathbf{R}_w\right]\ d\zeta = 0, \tag{1}$$

see, e.g., Wempner (1981).

Here γ and κ are the ring's mid-plane strain and bending measures (see Appendix A) and $\mathbf{f} = \mathbf{f}^*/K$ is the load vector, non-dimensionalised by the ring's bending stiffness $K = E\ (h/R_0)^3/[12(1-\nu^2)]$, where E and ν are the ring's elastic modulus and Poisson ratio, respectively. Time is non-dimensionalised by the fluid time-scale $t = t^*/T$ where $T = \mu R_0/\sigma^*$ (see below) and

$$\lambda_T = \frac{T_w}{T} = \frac{\sigma^*}{\mu}\sqrt{\frac{\rho_w}{K}} \tag{2}$$

represents the ratio of the time-scale $T_w = R_0\sqrt{\rho_w/K}$ for bending oscillations of the ring to the time-scale T for the surface-tension-driven redistribution of fluid in the liquid lining.

Carrying out the variations with respect to the displacements v^i and their derivatives transforms equation (1) into a variational equation of the form

$$\int_0^{2\pi} \left(\phi_i^{(0)}\ \delta v^i + \phi_i^{(1)}\ \delta v^i_{,\zeta} + \phi_i^{(2)}\ \delta v^i_{,\zeta\zeta}\right)\ d\zeta = 0, \tag{3}$$

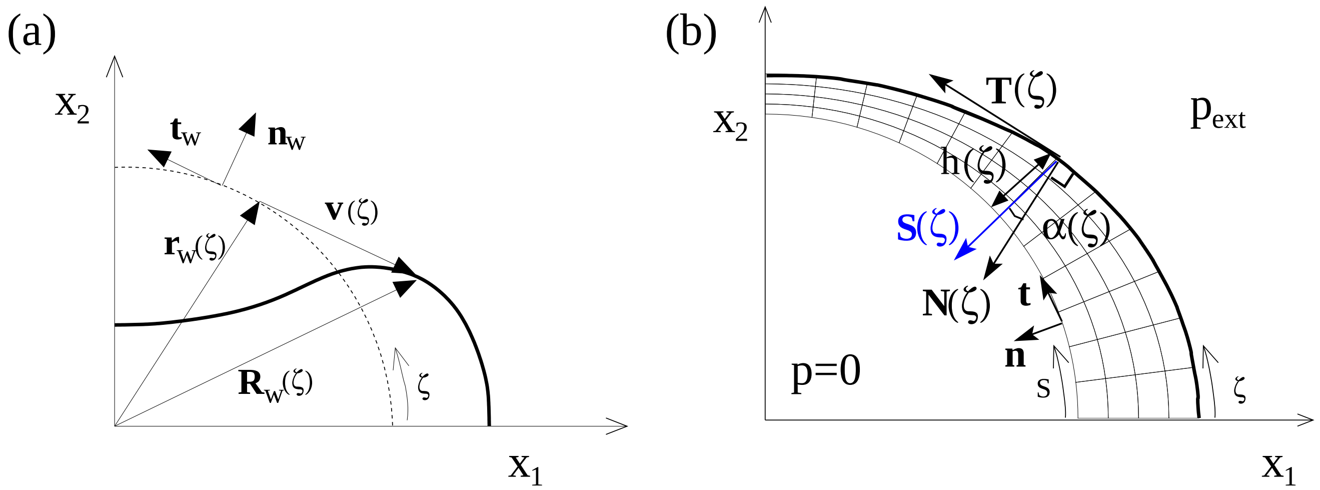

Figure 1: (a) Sketch of the wall deformation: a material point at $\mathbf{r}_w(\zeta)$ on the undeformed ring (dotted) is displaced by the displacement field $\mathbf{v}(\zeta)$ to a new position $\mathbf{R}_w(\zeta)$ on the deformed ring (solid). $\mathbf{t}_w$ and $\mathbf{n}_w$ are the unit tangent and normal vectors on the undeformed wall, respectively, and ζ is the Lagrangian coordinate along the ring's centreline. (b) Sketch illustrating the automatic fluid mesh generation in a (slightly less collapsed) ring: the nodal points are spaced uniformly along the spines $\mathbf{S}(\zeta)$ which emanate from the deformed wall and form an angle α with the inner wall normal $\mathbf{N}(\zeta)$. The free surface is parametrised by its 'height' $h(\zeta)$ along the spine. $\mathbf{T}(\zeta)$ is the unit tangent to the deformed wall and $\mathbf{t}$ and $\mathbf{n}$ are the unit tangent and normal vectors to the free surface, the arclength along which is given by S.

where commas denote partial derivatives. The summation convention is used and, unless stated otherwise, all subscripts range from 1 to 2. We exploit the symmetry of the two-lobed configuration and discretise only one quarter of the ring by displacement-based finite elements. The ϕ-terms contain up to second derivatives of the displacements, therefore we need shape functions with continuous first derivatives across the element boundaries. Isoparametric Hermite elements with nodal displacements and slopes as independent degrees of freedom (Bogner *et al.*, 1967) were chosen such that the displacements v^i were interpolated as

$$v^i = \sum_{j,k} V^{ijk} \psi_{jk}, \tag{4}$$

where the ψ_{jk} are piecewise Hermite polynomials. In terms of the local node numbers and the local element coordinate, $s \in [0,1]$, these shape functions are given by $\psi_{11}(s) = 2s^3 - 3s^2 + 1$, $\psi_{12}(s) = s^3 - 2s^2 + s$, $\psi_{21}(s) = -(2s^3 - 3s^2)$ and $\psi_{22}(s) = s^3 - s^2$. The first index of the shape function ψ_{jk} represents the local node number ($j = 1,2$); the shape function's second index ($k = 1,2$) represents the type of degree of freedom, interpolating the displacement or the derivative with respect to the local coordinate s, respectively. The time-derivative was discretised by the Newmark method (see, e.g., Bathe, 1996).

To generate isoparametric elements, the same shape functions were used to map the local coordinate s to the global Lagrangian coordinate ζ,

$$\zeta = \sum_{j,k} Z^{jk} \psi_{jk}. \tag{5}$$

Details of the choice of the coefficients Z^{jk} can be found in Heil & Pedley (1996).

We insert (4) and (5) into (3) and obtain

$$\left\{ \int_0^{\pi/2} \left(\phi_i^{(0)} \ \psi_{jk} + \phi_i^{(1)} \ \psi_{jk,\zeta} + \phi_i^{(2)} \ \psi_{jk,\zeta\zeta} \right) \ d\zeta \right\} \delta V^{ijk} = 0. \tag{6}$$

The variations of those V^{ijk} which are not determined by the symmetry conditions are arbitrary and the expressions multiplied by the corresponding δV^{ijk} have to vanish. This provides a system of non-linear algebraic equations for the unknown V^{ijk}. These equations still contain the load terms $\mathbf{f}$, which have to be determined from the solution of the fluid equations. The integrals over the elements were evaluated by Gaussian quadrature using at least 3 integration points (more points were used in regions of large pressure gradients).

2.2 The fluid equations

2.2.1 Navier-Stokes

The surface-tension-driven flow in the liquid lining is governed by the non-dimensional Navier-Stokes equations

$$Re \left(\frac{\partial u_i}{\partial t} + u_j \frac{\partial u_i}{\partial x_j} \right) = -\frac{\partial p}{\partial x_i} + \frac{\partial}{\partial x_j} \left(\frac{\partial u_i}{\partial x_j} + \frac{\partial u_j}{\partial x_i} \right) \tag{7}$$

and

$$\frac{\partial u_i}{\partial x_i} = 0. \tag{8}$$

The velocity scale U in the problem is set by the balance of surface tension and viscous effects, i.e. $U = \sigma^*/\mu$. This scale was used to non-dimensionalise the velocities, $u_i = u_i^*/U$. The Cartesian coordinates $x_i^* = R_0 x_i$ and all lengths were scaled on the ring radius R_0 which determines the fluid time-scale $T = R_0/U = R_0\mu/\sigma^*$ already referred to earlier. The corresponding Reynolds number is $Re = \rho R_0 U/\mu = \rho\sigma^* R_0/\mu^2$. Using this non-dimensionalisation, the viscous pressure scale is equal to the capillary pressure scale and we have $p = p^* R_0/\sigma^* = p^* R_0/(\mu U)$.

At the free air-liquid interface, whose position is described by the position vector $\mathbf{R}_h$, we have the kinematic free-surface condition

$$\mathbf{u} \cdot \mathbf{n} = \frac{\partial \mathbf{R}_h}{\partial t} \cdot \mathbf{n} \quad \text{at the air-liquid interface,} \tag{9}$$

and the dynamic boundary condition

$$-p n_i + \left(\frac{\partial u_i}{\partial x_j} + \frac{\partial u_j}{\partial x_i} \right) n_j - \ \kappa_h n_i = 0 \quad \text{at the air-liquid interface,} \tag{10}$$

where $\mathbf{n}$ is the outer unit normal on the air-liquid interface whose non-dimensional curvature is given by $\kappa_h = R_0 \kappa_h^*$.

The numerical technique employed to solve the Navier-Stokes equations on the variable domain enclosed by the free air-liquid interface and the deforming wall is illustrated in Fig. 1(b). We decompose the fluid domain into finite elements whose nodal positions are determined by the method of spines (Kistler & Scriven, 1983). For this purpose we parameterise the free surface position by its distance $h(\zeta)$ from the wall. The distance is measured in the direction of certain pre-determined unit vectors $\mathbf{S}$ (the spines) which form an angle α with the inner normal $\mathbf{N}$ on the wall. Since the spines emanate from given material points, we use the Lagrangian wall coordinate ζ to parameterise the free surface as

$$\mathbf{R}_h(\zeta) = \mathbf{R}_w(\zeta) + h(\zeta)\ \mathbf{S}(\zeta). \tag{11}$$

The spines not only resolve the free surface position but also facilitate the automatic adjustment of the fluid mesh to changes in the fluid domain: we associate each nodal point j in the fluid mesh with a fixed material point on the wall and identify it by its Lagrangian coordinate $\zeta_j^{(ref)}$. As the wall and the free surface deform, the fluid node remains located at a fixed, predetermined fraction $\omega_j \in [0,1]$ along its spine such that the position vector to fluid node j is given by

$$\mathbf{R}_j = \mathbf{R}_w(\zeta_j^{(ref)}) + \omega_j\ h(\zeta_j^{(ref)})\ \mathbf{S}(\zeta_j^{(ref)}). \tag{12}$$

We discretise the fluid equations with standard isoparametric Taylor-Hood type elements (Taylor & Hood 1973) so that the velocities, the global coordinates and the pressure are represented by

$$u_i = \sum_j U^{ij} \psi_j^{(F)}, \qquad x_i = \sum_j X^{ij} \psi_j^{(F)} \quad \text{and} \quad p = \sum_j P^j \psi_j^{(P)}, \tag{13}$$

where the $\psi_j^{(F)}$ and $\psi_j^{(P)}$ are bi-quadratic and bi-linear shape functions in the local element coordinates, respectively. X^{ij} are the nodal coordinates, given by (12). The free surface height $h(\zeta)$ and the spine angle $\alpha(\zeta)$ are discretised by one-dimensional isoparametric quadratic elements:

$$h = \sum_j H^j \psi_j^{(H)}, \quad \alpha = \sum_j A^j \psi_j^{(H)} \quad \text{and} \quad \zeta = \sum_j \tilde{Z}^j \psi_j^{(H)}, \tag{14}$$

where $\tilde{Z}^j = \zeta_j^{(ref)}$ and the $\psi_j^{(H)}$ are one-dimensional piecewise quadratic shape functions.

The residuals of the momentum equations (7) are weighted by the velocity shape functions $\psi_l^{(F)}$ and the dynamic boundary condition (10) is incorporated by partial integration (Ruschak, 1980). This yields

$$f_{il}^{(F)} = \int\int \left[Re \left(\frac{\partial u_i}{\partial t} + (u_j - u_j^{(M)}) \frac{\partial u_i}{\partial x_j} \right) \psi_l^{(F)} - p \frac{\partial \psi_l^{(F)}}{\partial x_i} + \left(\frac{\partial u_i}{\partial x_j} + \frac{\partial u_j}{\partial x_i} \right) \frac{\partial \psi_l^{(F)}}{\partial x_j} \right] dv$$

$$- \int t_i\ \frac{\partial \psi_l^{(F)}}{\partial S}\ dS = 0, \tag{15}$$

where $\int\int dv$ is the integral over the fluid domain, S is the arc-length along the free surface, t_i represents the components of its unit tangent vector and

$$u_j^{(M)} = \sum_j \frac{\partial X^{ij}}{\partial t} \psi_j^{(F)} \tag{16}$$

is the mesh velocity. The time-derivative was evaluated by a second-order backward Euler scheme (BDF2). The fully implicit treatment of the momentum equations leads to a consistent mass representation. Similarly, the continuity equation (8) is weighted with the bilinear pressure shape functions $\psi_l^{(P)}$ which yields

$$f_l^{(P)} = \int\int \frac{\partial u_j}{\partial x_j} \psi_l^{(P)} dv = 0. \tag{17}$$

Weighting the kinematic free surface condition (9) by the one-dimensional quadratic shape functions $\psi_l^{(H)}$ provides the equations which determine the unknown free surface heights H^j via

$$f_j^{(H)} = \int \left(\mathbf{u} - \frac{\partial \mathbf{R}_h}{\partial t} \right) \cdot \mathbf{n} \ \psi_j^{(H)} dS = 0. \tag{18}$$

Finally, the discrete spine angles A^j were determined by algebraic conditions which ensured that the spines did not intersect inside the fluid domain. A suitable set of equations was generated by assuming that the spines behave like rigid rods which pivot about the material points on the wall and are connected to neighbouring spines by nonlinear springs, attached at the free ends. The equilibrium equations of this mechanical system provide a sufficient number of equations to determine the A^j. The nonlinearity of the springs ensures that the end points of the spines are kept apart.

2.2.2 Lubrication theory

If the non-dimensional film thickness is small, i.e. $h = h^*/R_0 \ll 1$, and if h varies slowly along the ring's gently curved circumference, such that $|dh/d\zeta| \ll 1$, as in Fig. 2(a), the flow in the liquid lining can be approximated by lubrication theory, i.e.

$$\frac{\partial h}{\partial t} + \frac{\partial}{\partial \xi} \left(\frac{h^3}{3} \frac{\partial \kappa_h^{(lin)}}{\partial \xi} \right) = 0, \tag{19}$$

where $d\xi = |\partial \mathbf{R}_w / \partial \zeta| \ d\zeta$ is the arc-length along the (slightly) stretched ring centre-line and $\kappa_h^{(lin)}$ is the non-dimensional curvature of the air-liquid interface, linearised with respect to the wall displacements and the film thickness h; see e.g. Schwartz & Weidner (1995). A rescaling of h in (19) by the typical film thickness H_0^* shows that the time-scale for the redistribution of the fluid on the curved substrate is given by $T_L = (R_0/H_0^*)^3 \mu R_0/\sigma^* \gg T$ which corresponds to a velocity scale of $U_L = (H_0^*/R_0)^3 \sigma^*/\mu \ll U$ and a Reynolds number of $Re_L = (H_0^*/R_0)^3 \rho R_0 \sigma^*/\mu^2 \ll Re$.

Lubrication theory can be expected to provide an accurate description of the surface-tension-driven redistribution of fluid during the early stages of the ring's buckling. However, the assumptions underlying its derivation from the full Navier-Stokes equations are unlikely to be fulfilled during the later stages when the ring has

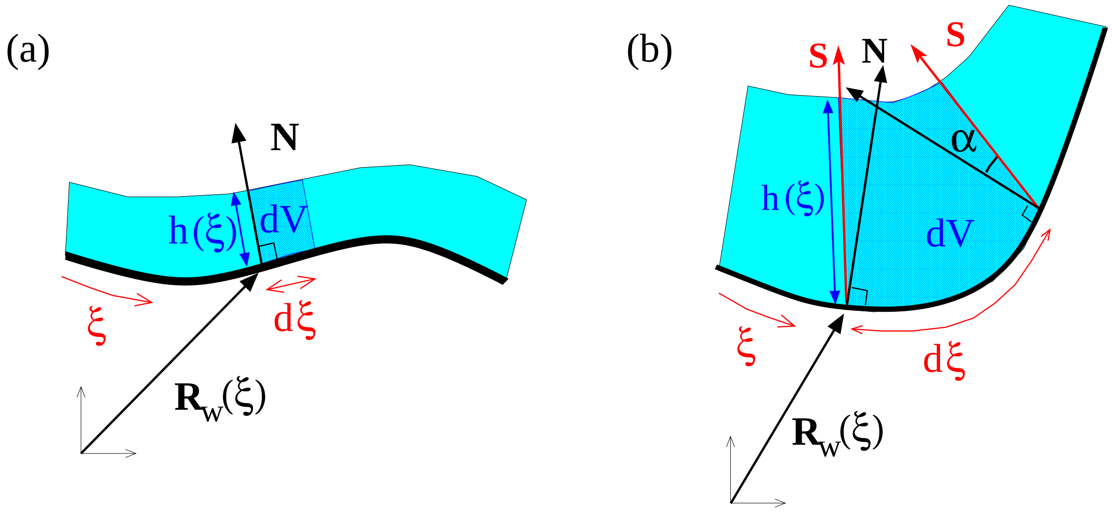

Figure 2: (a) Thin film on a gently curved substrate: the free surface can be parametrised by $\mathbf{R}_h(\xi) = \mathbf{R}_w(\xi) + h(\xi)\ \mathbf{N}(\xi)$ and $dV \approx h\ d\xi$. (b) Thick film on a strongly curved substrate: the wall normals $\mathbf{N}$ can intersect inside the fluid domain and $dV \not\approx h\ d\xi$. The free surface is instead parametrised by $\mathbf{R}_h(\xi) = \mathbf{R}_w(\xi) + h(\xi)\ \mathbf{S}(\xi)$ where the spines $\mathbf{S}(\xi)$ form an angle $\alpha(\xi)$ with the normals on the wall.

buckled strongly and the film thickness has become large and strongly non-uniform. Use of lubrication theory in such situations leads to a number of problems, which are illustrated in Fig. 2(b): **(i)** the approximation of the interface curvature κ_h by its linearisation $\kappa_h^{(lin.)}$ becomes inaccurate; **(ii)** the derivation of equation (19) assumes that the film thickness, h, is measured in the direction normal to the substrate, implying a parametrisation of the air-liquid interface as $\mathbf{R}_h(\xi) = \mathbf{R}_w(\xi) + h(\xi)\ \mathbf{N}(\xi)$. For thick films on strongly curved substrates, this definition of a film thickness becomes somewhat ambiguous. Furthermore, the parametrisation of the air-liquid interface breaks down if the wall normals intersect inside the fluid domain; **(iii)** lubrication theory assumes that the substrate and interface curvatures are so small that the volume dV of fluid 'above' a length $d\xi$ of substrate can be approximated by $dV \approx h\ d\xi$. For thick films on strongly curved substrates, this approximation becomes very poor and the numerical computations shown below indicate that this lack of volume conservation in lubrication theory is the main reason for its poor performance in 'thick film regions'.

We shall now introduce a number of modifications to the lubrication theory model (19) that will address these problems: **(i)** following Gauglitz & Radke (1988), we use the exact, fully non-linear expression for the curvature κ_h in terms of the film thickness and the wall displacement field, even though, from an asymptotic point of view, the linearised expression for the curvature would be sufficient. In many applications (e.g. Halpern & Grotberg 1992, Johnson *et al.* 1991, Weidner *et al.* 1997, Jensen 2000) this approach has been shown to significantly improve the accuracy of the lubrication theory model. This is because the system evolves towards equilibrium states which are characterised by constant curvature of the air-liquid interface. The use of the exact curvature ensures that these equilibrium states are represented correctly (provided the substrate curvature is small; see below). **(ii)** To extend the computations beyond situations in which the wall normals intersect inside the fluid domain, we represent the free surface position $\mathbf{R}_h$ by the method of spines (11) via $\mathbf{R}_h(\xi) = \mathbf{R}_w(\xi) + h(\xi)\ \mathbf{S}(\xi)$, as illustrated in Fig. 2(b). Using the technique described in section 2.2.1, we adjust the spine angles $\alpha(\xi)$ such that the spines remain approximately normal in regions of small film thickness (where lubrication theory remains applicable) while we allow them to rotate sufficiently to avoid intersection in regions of large film thickness. **(iii)** Using the spine-based parametrisation of the air-liquid interface, we use elementary differential geometry to determine the exact volume dV of fluid 'above' a length $d\xi$ of substrate, $dV = M\ d\xi$, where

$$M(\xi) = \int_0^{h(\xi)} \left| \frac{\partial \mathbf{R}_w}{\partial \xi} + \theta\ \frac{\partial \mathbf{S}}{\partial \xi} \right| d\theta. \tag{20}$$

Inserting this into the mass balance underlying the derivation of equation (19) then yields the modified evolution equation

$$\frac{\partial M}{\partial t} + \frac{\partial}{\partial \xi}\left(\frac{h^3}{3} \frac{\partial \kappa_h}{\partial \xi} \right) = 0. \tag{21}$$

Note that in regions of small substrate curvature, where we choose $\mathbf{S} \approx \mathbf{N}$, we have $|\partial \mathbf{S}/\partial \xi| \ll |\partial \mathbf{R}_w/\partial \xi|$. Hence, we recover $\partial M/\partial t \approx \partial h/\partial t$, as in (19), in regions where classical lubrication theory is valid.

It must be stressed that the modifications introduced above are not 'rational' in the sense of a long-wavelength asymptotic theory. They do, however, present a necessary extension of Gauglitz & Radke's (1988) (equally non-rational) method to situations in which the substrate curvature is large. Surface-tension-driven flows evolve towards equilibrium states of constant interface curvature while conserving the volume of fluid. On a flat substrate, classical lubrication theory is exactly volume conserving, therefore the use of the exact interface curvature in (19) ensures that the the system's equilibrium states are represented correctly. For flows on strongly curved substrates, volume conservation needs to be explicitly incorporated into the model. In our formulation this is achieved by equation (20).

The numerical solution of (21) is no more difficult than the solution of (19) but significantly easier than the solution of the full Navier-Stokes equations. The only complication arises (in both formulations) from the fact that (19) and (21) involve the second derivative of the interface curvature κ_h which itself contains second derivatives of the wall displacement field v^i. Fourth derivatives of the wall displacement field are not available from the Hermite expansion in (4). Therefore, equation (21) was solved by a mixed finite element method in which independent Hermite interpolations for the film's thickness and its curvature were used, i.e.

$$h = \sum_{j,k} H^{jk} \psi_{jk} \quad \text{and} \quad \tilde{\kappa}_h = \sum_{j,k} K^{jk} \psi_{jk}. \tag{22a, b}$$

The finite element expansion (22b) for the film curvature was then used in the Galerkin solution of the weak form of (21) which was integrated by parts to yield the equations

$$f_{jk}^{(H)} = \int_0^{\pi/2} \left(\frac{\partial M}{\partial t} \psi_{jk} - \frac{h^3}{3}\ \frac{\partial \tilde{\kappa}_h}{\partial \xi}\ \frac{\partial \psi_{jk}}{\partial \xi} \right) d\zeta = 0. \tag{23}$$

After discretising the time-derivative by a second-order backward Euler scheme (BDF2), this provides a system of discrete equations for those H^{jk} which are not determined by the symmetry conditions. The equations were augmented by the weak equations for the discrete curvatures K^{jk}

$$f_{jk}^{(K)} = \int_0^{\pi/2} \left(\sum_{l,m} K^{lm} \psi_{lm} - \kappa_h \right) \psi_{jk} \; d\zeta = 0, \tag{24}$$

where κ_h is the exact curvature of the air-liquid interface.

2.3 Fluid-solid interaction

The fluid and solid domains interact via the no-slip condition

$$\mathbf{u} = \frac{\partial \mathbf{R}_w}{\partial t} \quad \text{on the wall,} \tag{25}$$

and via the traction that the fluid exerts onto the wall; the latter implies that the load terms in the wall equations are given by

$$f_i = p_{ext} \; N_i + \sigma \left[-p \; \delta_{ij} + \left(\frac{\partial u_i}{\partial x_j} + \frac{\partial u_j}{\partial x_i} \right) \right] N_j, \tag{26}$$

for the Navier-Stokes model and

$$\mathbf{f} = p_{ext} \; \mathbf{N} + \sigma \left(\kappa_h \; \mathbf{N} + \; h \; \frac{d\kappa_h}{d\xi} \; \mathbf{T} \right) \tag{27}$$

for the lubrication theory model. $\mathbf{T}$ and $\mathbf{N}$ are the unit tangent and the unit inner normal on the deformed ring, respectively (see Fig. 1b), and

$$\sigma = \frac{\sigma^*}{R_0 \; K} \tag{28}$$

is the non-dimensional surface tension which represents the ratio of the surface tension forces to the wall's bending stiffness.

The discretised fluid and solid equations were combined into a coupled system of non-linear algebraic equations which was solved by Newton's method. The large, sparse but poorly structured Jacobian matrix was generated by finite differencing, taking the sparsity pattern of the matrix into account. The linear systems were solved by Demmel *et al.*'s (1999) SuperLU solver with minimum degree ordering of the equations. A basic adaptive time-stepping procedure was employed to increase the temporal resolution in periods of rapid change: the time-step was halved whenever any of the discrete wall displacements or film thicknesses changed by more than a critical threshold Δ_{max} per time-step. ($\Delta_{max} = 10^{-2}$ was used in most computations). Thus, the slowly varying changes during the early stages of the system's evolution could be resolved with relatively large time-steps (usually $\Delta t = 0.1$) while the rapid changes during the later stages were resolved accurately by employing much smaller time-steps (down to $\Delta t = 10^{-7}$). Regions of the fluid domain which tended to develop into thin films were discretised by a larger number of elements to resolve the large pressure variations in the resulting draining flows. We also used a larger number of integration points for the shell elements in these regions.

A variety of tests were carried out to validate the code: we compared the static ring deformation and the value of p_{ext} at which opposite wall contact occurs for the first time to the predictions of Flaherty *et al.*'s (1972) inextensible Euler-Bernoulli model (see also Appendix D) and compared the ring's small amplitude oscillations to the eigenmodes predicted by linear theory (Soedel 1993). The newly developed time-dependent Navier-Stokes solver was validated by prescribing a wall displacement field (and thus, via (25), the velocity boundary conditions) for which a divergence-free extension of the velocity field into the interior of the fluid domain could easily be found. To make this velocity field an exact solution of the Navier-Stokes equations, an appropriate body force term was added to the discretised momentum equations (15). For all validation cases, excellent agreement between the exact and the numerical solutions was obtained. Further validation was provided by the comparison between the independently developed lubrication theory and Navier-Stokes solvers (see section 3.3). Finally, the mesh independence of the results was confirmed by repeating selected runs with a finer spatial resolution [increasing the number of degrees of freedom from the standard resolution of ≈ 1700 (for 160 fluid and 10 wall elements) to ≈ 3500 (for 350 fluid and 20 wall elements)] and with reduced time-steps (by reducing the initial time-step to $\Delta t = 10^{-3}$ and the threshold for the time-step reduction to $\Delta_{max} = 10^{-3}$; see Fig. 12). For the standard resolution, a converged solution was typically obtained within 3-4 Newton iterations, which required approximately 2 minutes of CPU time on a DEC Alpha 433au workstation.

3 Results

Before presenting results, we summarise the non-dimensional parameters which govern the problem: the non-dimensional surface tension $\sigma = \sigma^*/(R_0 K)$ represents the ratio of surface tension forces to the wall's bending stiffness. The Reynolds number (on the lubrication theory scale) is given by

$$Re_L = \left(\frac{H_0^*}{R_0}\right)^3 \frac{R_0 \rho \sigma^*}{\mu^2}$$

while

$$\lambda_T = \frac{\sigma^*}{\mu}\sqrt{\frac{\rho_w}{K}} \quad \text{and} \quad \Lambda_T = \left(\frac{H_0^*}{R_0}\right)^3 \frac{\sigma^*}{\mu}\sqrt{\frac{\rho_w}{K}}$$

represent the ratio of the fluid time-scale (on the Stokes and lubrication theory scales, respectively) to the time-scale for the wall's bending oscillations. The two final parameters are the non-dimensional wall thickness h/R_0 and the non-dimensional initial film thickness H_0^*/R_0.

All results in this paper were obtained for a non-dimensional wall thickness of $h/R_0 = 1/20$. This value was chosen as a compromise between the values in the lung airways (which tend to be slightly thicker) and the limitations imposed by the use of thin-shell theory. All other parameters were chosen to lie in a physiologically realistic range, discussed in more detail in section 4.

3.1 Linear instability

A lengthy but straightforward normal mode analysis of the lubrication theory equations (19), coupled to Sanders's (1963) moderate rotation approximation to the

Euler-Lagrange equations of the variational principle (1) yields the following results (see Appendix B for further details). For a given value of the non-dimensional surface tension σ, the external pressure at which the system's axisymmetric state becomes unstable to non-axisymmetric perturbations of the form

$$\mathbf{v}(\zeta,t), h(\zeta,t) \sim \exp(iN\zeta + \frac{\omega}{\lambda_T}\, t) \tag{29}$$

is given by

$$p_{ext}^{(buckl)} = N^2 - 1 - \frac{\sigma}{(1-H_0)} \tag{30}$$

This shows that $N = 2$ is the most unstable mode and that an instability (i.e. $Re(\omega) > 0$) occurs when the combined compression of the external pressure and the surface tension exceeds the ring's classical buckling pressure $p_{ext}^{(buckl)}(\sigma = 0) = N^2 - 1$. Hence an increase in surface tension is destabilising in that it lowers the buckling pressure of the ring. This was already shown by Rosenzweig & Jensen (2001) whose static stability analysis also revealed that the character of the static bifurcation changes from super- to sub-critical when σ exceeds the critical value

$$\sigma_{crit} = \frac{3}{2}\,\frac{(N^2-1)^2}{N^2}\,(1-H_0)^3. \tag{31}$$

Having established that an increase in surface tension destabilises the system, we shall now investigate its behaviour following an increase in p_{ext} above the buckling pressure. In order to make meaningful comparisons between results of parameter studies using different values of σ and H_0, we shall subject all rings to the same excess pressure

$$p_{exc} = p_{ext} - p_{ext}^{(buckl)}(\sigma, H_0) = 0.05 \tag{32}$$

above the buckling pressure. Note that, in the absence of the fluid layer, this excess pressure would cause the ring to buckle slightly into an approximately elliptical shape with a maximum radial displacement of $v_{max}^2 = -0.153$ at the point of strongest inward collapse. A few computations were performed with other values of p_{exc}. The system's qualitative behaviour remained unchanged from that shown below, provided p_{exc} did not become so large that the external pressure completely dominated the ring's compression.

Fig. 3 shows the growth rate $Re(\omega)$ of the non-axisymmetric instability as a function of the non-dimensional surface tension σ for various values of the initial film thickness H_0. For $\sigma = 0$, the fluid does not affect the ring's deformation and the system undergoes a purely elastic instability while the fluid passively redistributes itself on the buckling ring. (Note that the limit $\sigma = \sigma^*/(KR_0) \to 0$ is to be understood as the limit in which $\sigma^*/R_0 \ll K$, i.e. the surface-tension-induced pressure variations in the fluid become much smaller than the ring's bending stiffness). The growth rate in (29) is scaled on the ring time-scale T_w, therefore $Re(\omega)$ at $\sigma = 0$ is independent of the initial film thickness H_0.

To explain the variations of the growth rate $Re(\omega)$ with an increase in non-dimensional surface tension, shown in Fig. 3(a), we compare the pressure distribution just before the loss of stability (at $t = t_0$) to that shortly after the onset of buckling (at $t = t_0 + \Delta t$): at $t = t_0$, the ring is subject to a spatially uniform compression which consists of the external pressure and the compressive load due to

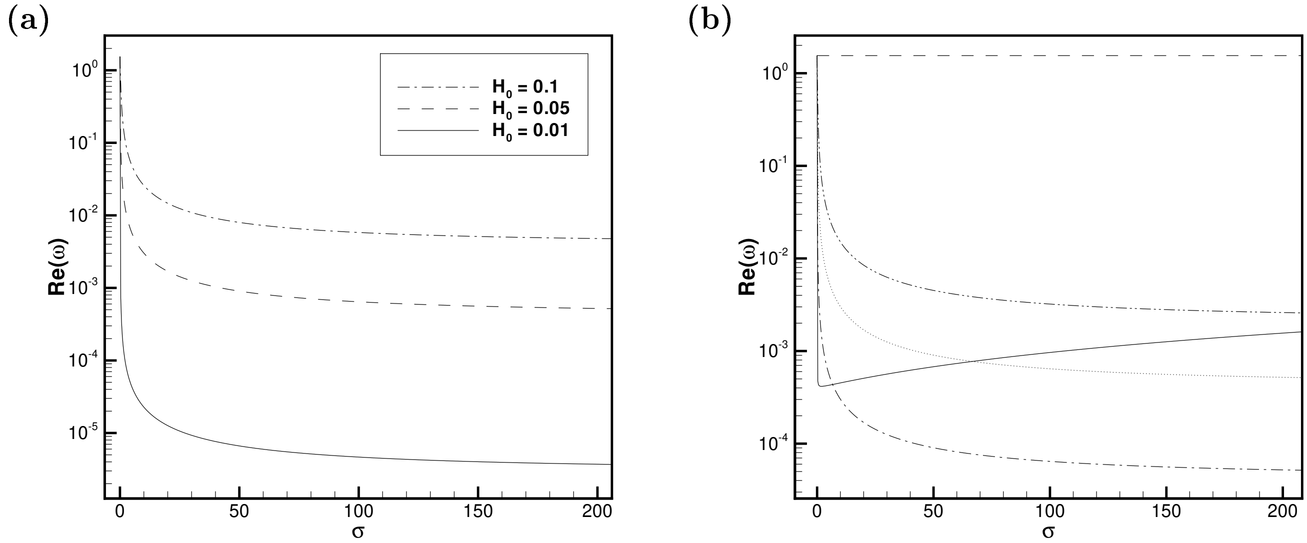

Figure 3: The non-dimensional growth rate $Re(\omega)$ of the non-axisymmetric instability versus the non-dimensional surface tension. Note that ω is scaled on the ring time-scale, i.e. $\omega = \omega^* T_w$. (a) Effect of different film thicknesses: $H_0 = 0.01$ (solid; $\sigma_{crit} = 3.27$), $H_0 = 0.05$ (dashed; $\sigma_{crit} = 2.89$) and $H_0 = 0.1$ (dash-dot; $\sigma_{crit} = 2.46$). $\lambda_T = 10^3$ in all cases. (b) Effect of variations in the time-scale ratio: $\lambda_T = 10^2$ (dash-dot), $\lambda_T = 10^3$ (dotted), $\lambda_T = 5 \times 10^3$ (dash-dot-dot) and $\lambda_T \to \infty$ (dashed). The solid line corresponds to the case $\lambda_T/\sigma = 15$ and represents the variations of the growth rate with changes in the dimensional surface tension σ^*. $H_0 = 0.05$ for all cases.

the surface tension of the liquid lining (see Fig. 4a). As the ring buckles, the curvature of the air-liquid interface becomes non-uniform and the resulting curvature gradient induces a tangential pressure gradient in the liquid film. This pressure gradient drives fluid into the buckling lobe and attempts to keep the air-liquid interface axisymmetric. The surface-tension-induced pressure distribution also opposes the wall deformation because the reduced fluid pressure in the buckling lobes pulls them back towards the centre. At larger σ, the fluid pressure provides a greater contribution to the load on the wall [see (26) and (27)]. Hence, an increase in σ increases the stabilising effect of the non-uniform fluid pressure distribution, as shown in Fig. 4(b), and thus reduces the growth rate of the non-axisymmetric instability.

For a given value of the surface tension, fluid in thicker films redistributes itself more rapidly in response to changes of the interfacial curvature. Hence, for thicker films, the curvature of the air-liquid interface remains more uniform while the ring buckles and the tendency of the surface-tension-induced pressure distribution to oppose the ring's non-axisymmetric deformation is reduced. This effect is responsible for the increase in $Re(\omega)$ with H_0, shown in Fig. 3(a). The figure also shows that at sufficiently large surface tension, $Re(\omega) \sim H_0^3$, which indicates that the dynamics of the instability are controlled by the surface-tension-driven redistribution of the fluid in the liquid lining. This may be confirmed by comparing the growth rates in Fig. 3(a) to those obtained from an analysis in which wall inertia is neglected (by

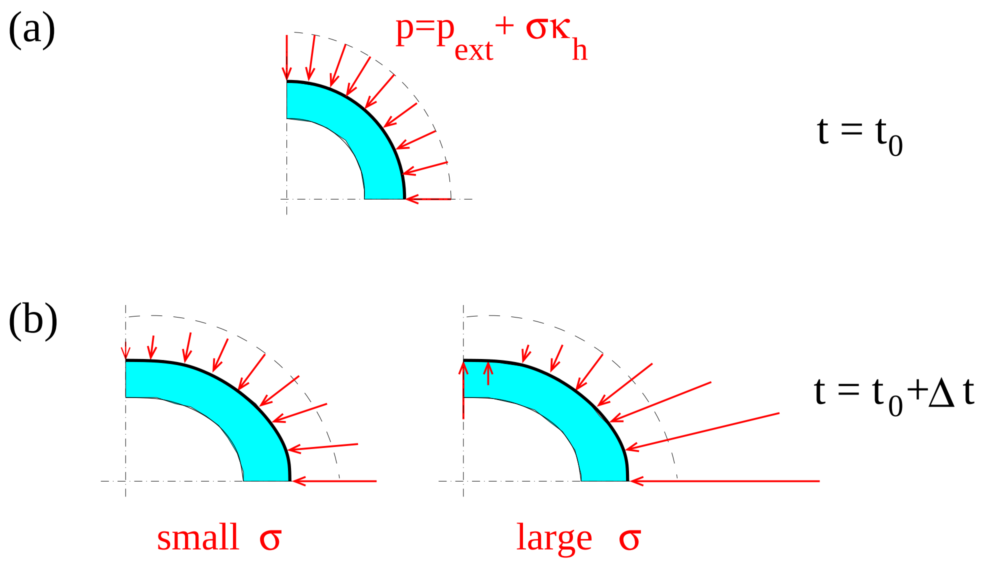

Figure 4: Sketch of the pressure acting on the ring before and after buckling. During buckling, p_{ext} remains constant whereas the fluid pressure whose magnitude is proportional to σ becomes more negative in the part of the ring that buckles outwards. This stabilising effect is more pronounced at larger non-dimensional surface tension.

setting the time-derivatives in the shell equations to zero). For the parameter values used in Fig. 3(a), the growth rates with and without wall inertia are practically indistinguishable – noticeable discrepancies only arise at values of H_0 which are too large to justify the use of lubrication theory and at very small values of the surface tension.

The broken lines in Fig. 3(b) show that an increase in the time-scale ratio λ_T increases the growth rate of the non-axisymmetric instability. This is because an increase in λ_T reduces the time-scale for the surface-tension-driven redistribution of fluid on the buckling ring. Similar to the effect of an increase in H_0, an increase in λ_T therefore reduces the departure of the air-liquid interface from its axisymmetric state and thus reduces the stabilising effect of the non-uniform fluid pressure distribution. For $\lambda_T \to \infty$, the fluid redistributes itself instantaneously and the air-liquid interface always remains axisymmetric. In this case, the growth rate of the instability becomes independent of σ and approaches the value for the ring without a fluid layer.

In the context of the airway closure problem, it is of interest to consider the effect of variations in the dimensional surface tension σ^*. For this purpose, it is important to realise that both σ and λ_T scale linearly with σ^*. Hence an increase σ^* requires $\lambda_T/\sigma = const.$ which results in a competition between two effects: the increase in σ tends to decrease the growth rate, while the accompanying increase in λ_T tends to increase it. The solid line in Fig. 3(b), which shows $Re(\omega)$ for $\lambda_T/\sigma = 15$, indicates that, at small values σ, the stabilising effect of an increase in σ dominates, whereas for larger values of σ, the increase in growth rate due to the increase in λ_T becomes more important.

3.2 Non-linear behaviour

We shall now use the numerical techniques described in section 2 to follow the instability into the large-displacement regime. Motivated by the results of the linear instability analysis, we initially neglect all inertia (by setting $\lambda_T = 0$ and $Re = 0$). The same initial conditions (representing an undeformed axisymmetric ring, lined with a liquid film of uniform thickness H_0) are used for all cases and all rings are subjected to the same excess pressure $p_{exc} = 0.05$. A small cosinusoidal pressure perturbation $p_{cos} = 10^{-4}\cos(2\zeta)$ was added to the load terms in the shell equations, to force the numerical solution from the axisymmetric state. We illustrate the system's non-axisymmetric evolution by plotting the radii of four control points (identified in Fig. 5a) on the wall and the air-liquid interface as a function of time.

3.2.1 Effect of variation in the surface tension

First, we investigate how the ring's post-buckling behaviour is affected by changes to the surface tension σ^*. Again, it is important to realise that an increase in σ^* not only increases the non-dimensional surface tension $\sigma = \sigma^*/(R_0 K)$ but also decreases the lubrication theory time-scale $T_L = (R_0/H_0)^3 \mu R_0/\sigma^*$ which, in the absence of inertia, is the only remaining time-scale in the problem. When investigating how changes in σ^* affect the temporal evolution of the system, it is therefore most instructive to present the results on a surface-tension-independent time-scale. In the current section, we will therefore non-dimensionalise time by $\hat{T}_L = \sigma T_L = (R_0/H_0)^3\ \mu/K$.

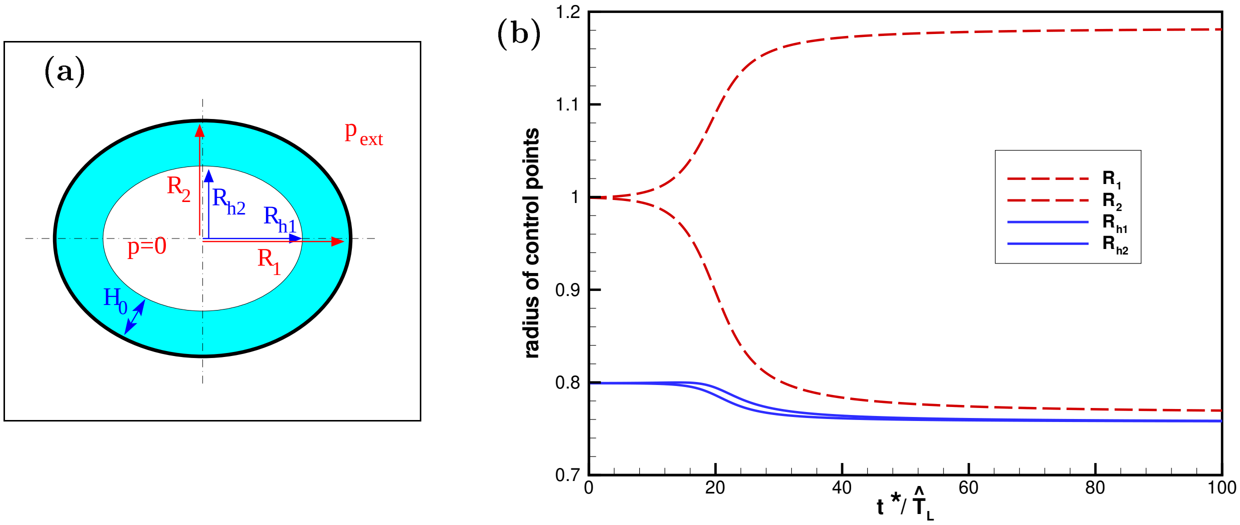

Figure 5: (a) Sketch of the control radii used to characterise the system's non-axisymmetric evolution. (b) Evolution of a liquid-lined ring for $H_0 = 0.2$ and $\sigma = 0.864 = 0.5\ \sigma_{crit}$.

Fig. 5 shows the evolution of an initially ($t = 0$) axisymmetric ring, lined with a uniform film of thickness $H_0 = 0.2$ (corresponding to $\sigma_{crit} = 1.728$ for $N = 2$) and relatively small surface tension $\sigma = 0.864 = 0.5\ \sigma_{crit}$. As the ring buckles non-axisymmetrically (R_2 decreases by about 20% while R_1 increases by a slightly smaller amount), the surface-tension-driven flow in the liquid lining attempts to keep the air-liquid interface axisymmetric ($R_{h1} \approx R_{h2}$, apart from the short period of time during which the ring buckles rapidly). Following the initial instability, the system approaches a new steady state. Fig. 6 illustrates the corresponding flow in the liquid lining: the slight non-axisymmetry of the air-liquid interface generates a pressure distribution which opposes the wall deformation and drives fluid towards the part of the ring that buckles outwards. In the final steady state, an axisymmetric air-liquid interface is contained inside the buckled ring. Note that, since the volume of fluid in the liquid lining is conserved, the reduction in the ring's cross sectional area during buckling translates into a reduction of the luminal area. Hence the curvature of the air-liquid interface, and with it the compressive load on the ring, increases slightly while the ring buckles. Compared to the case of a ring without a liquid lining, the maximum radial displacement increases to $v^2_{max} = -0.230$ at the point of strongest inward collapse.

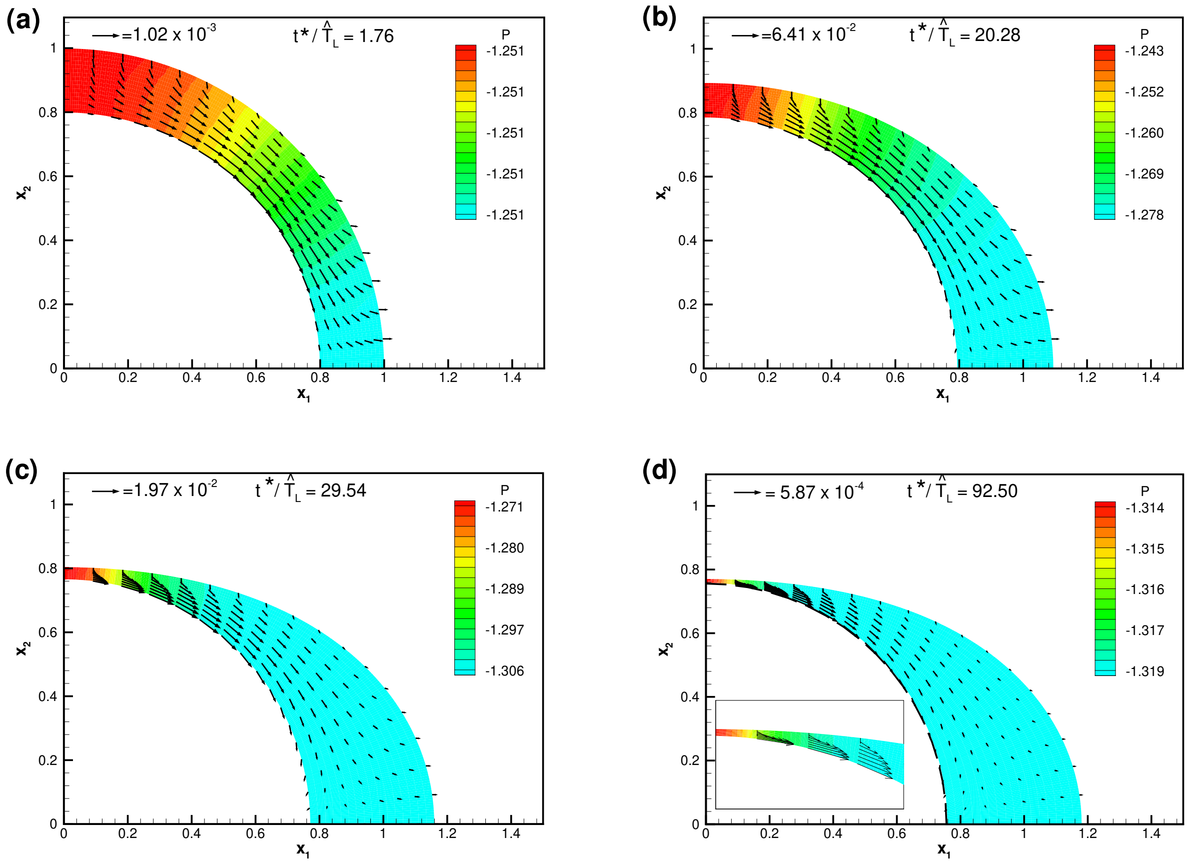

Figure 6: The shape of the fluid domain, the velocities and the pressure distribution for a buckling, liquid-lined ring; $H_0 = 0.2$, $\sigma = 0.5\,\sigma_{crit}$. Note the different scales for the vector lengths and pressure contours. The velocities are scaled on the lubrication scales. The inset shows the detail of the flow in the thin-film region. The dashed line in (d) represents a circle of radius R_{h2} and illustrates that the air-liquid interface has become nearly axisymmetric.

Fig. 7(a) compares the system's evolution for an increased non-dimensional surface tension of $\sigma = 2.5\ \sigma_{crit}$ to the behaviour at $\sigma = 0.5\ \sigma_{crit}$. We note that, as

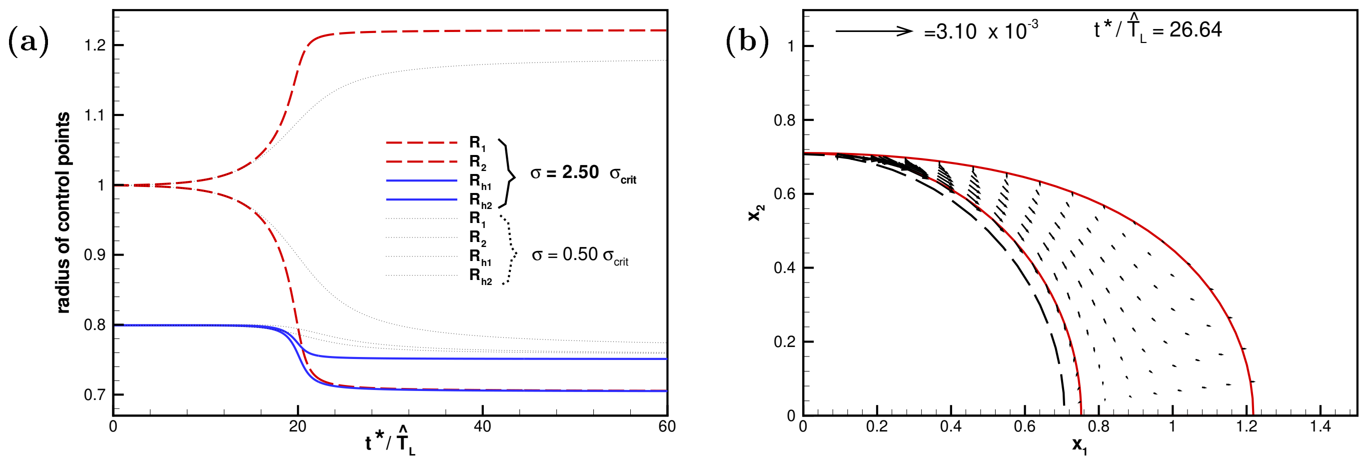

Figure 7: (a) Comparison of the evolution of two liquid-lined rings with $\sigma = 4.32 = 2.5\ \sigma_{crit}$ and $\sigma = 0.5\ \sigma_{crit}$, respectively. $H_0 = 0.2$ in both cases. (b) The shape of the fluid domain and the velocities (on the lubrication scale) at large times for $\sigma = 2.5\ \sigma_{crit}$: the system is not in equilibrium and fluid continues to drain slowly out of the thin-film region. The dashed line represents a circle of radius R_{h2} and illustrates that the air-liquid interface is not axisymmetric.

predicted by the linear instability analysis, the increase in dimensional surface tension σ^* slightly increases the initial growth rate of the instability. As before, surface tension tries to redistribute the fluid in order to maintain an axisymmetric air-liquid interface while the ring buckles. However, now the increase in the compressive load during buckling deforms the ring more strongly and it becomes impossible to 'fit' an axisymmetric air-liquid interface of the required curvature into the buckled ring. Hence, even though the large-time behaviour for $\sigma = 2.5\ \sigma_{crit}$, illustrated in Fig. 7(a), appears to be similar to that for $\sigma = 0.5\ \sigma_{crit}$, the system depicted in Fig. 7(b) is not in equilibrium: R_{h1} remains significantly larger than R_{h2}, indicating that the air-liquid interface is not axisymmetric as would be required for an equilibrium state. Hence fluid continues to drain from the ever-thinning thin-film region so that $h_2 = R_2 - R_{h2} \to 0$ as $t \to \infty$. In the real physical system, Van der Waals forces would ultimately rupture the film once its thickness is lower than a critical value (of the order of nanometers; see, e.g., Oron *et al.* 1997). After rupture, the system would approach one of Rosenzweig & Jensen's (2001) equilibrium configurations with partially dry walls. Film rupture and the subsequent contact line motion have not been included in the present model but the computations show that the film thinning takes place over very long times.

A further increase of the non-dimensional surface tension to $\sigma = 5.0\ \sigma_{crit}$ leads to a dramatic change in the system's behaviour, as illustrated in Fig. 8: initially, the increase in σ and σ^* merely leads to a further increase in the growth rate of

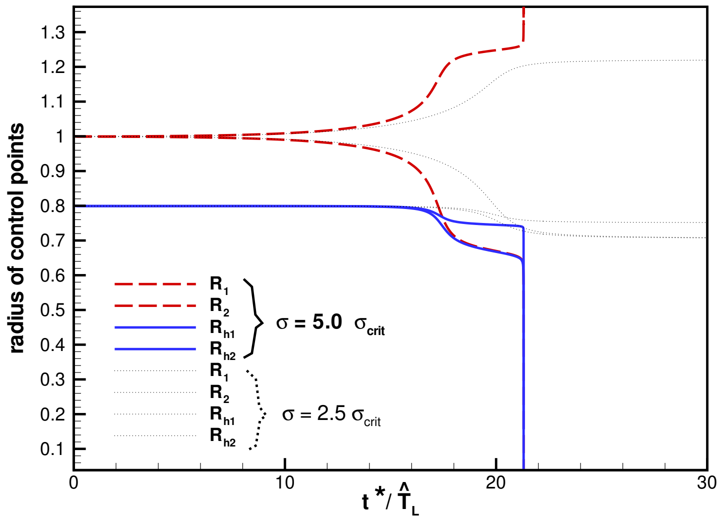

Figure 8: Comparison of the evolution of two liquid-lined rings for $\sigma = 8.64 = 5.0\ \sigma_{crit}$ and $\sigma = 2.5\ \sigma_{crit}$, respectively. $H_0 = 0.2$ in both cases.

the non-axisymmetric instability. However, at this value of the surface tension, the additional ring compression generated during the buckling process becomes so strong that the ring must undergo larger and larger deformations to generate the bending moments required to balance this compression. The larger deformations further reduce the radius of the air-liquid interface and thus further increase the ring compression. Ultimately, this results in a 'catastrophic' collapse (as $t^*/\hat{T}_L \to T_{clos} \approx 21.19$) during which the air-liquid interface shrinks to a point and the ring becomes completely occluded. Fig. 9 illustrates the corresponding flow field and the pressure distribution in the liquid lining: after the initial moderate buckling (Fig. 9a), the system temporarily settles into a slowly changing configuration in which fluid drains slowly from the thin-film region into the buckled lobe where the fluid pressure is approximately uniform (Fig. 9b). Fig. 9(c) shows the early stages of the final collapse during which the fluid velocity rapidly increases by several orders of magnitude. The air-liquid interface collapses inwards while continuously lowering the fluid pressure, thus further accelerating the ring collapse. The details of the very final stages of the collapse are complicated and difficult to resolve numerically but the end result is a completely occluded ring: in the context of the physiological problem we have airway closure despite the fact that the volume of fluid is insufficient to occlude the axisymmetric airway.

Finally, Fig. 10 shows that after a further increase in surface tension to $\sigma = 10.0\ \sigma_{crit}$, the increase in ring compression during the early stages of the buckling is already sufficient to initiate the final catastrophic collapse – the intermediate period, during which fluid drains slowly out of the thin-film region while the ring remains nearly stationary, disappears. This behaviour is representative of all larger values of the surface tension.

As mentioned above, the presentation of the results on a surface-tension-independent

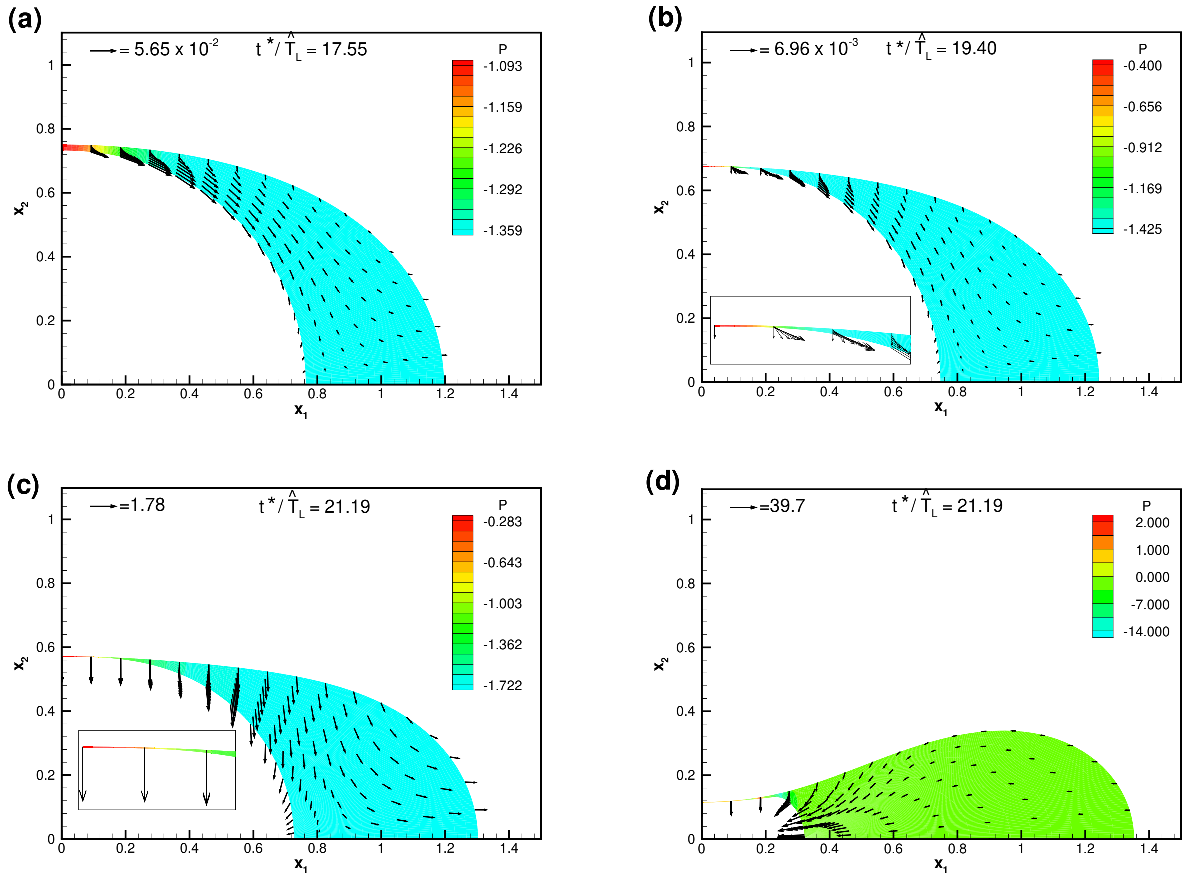

Figure 9: Collapse of a liquid-lined ring for $H_0 = 0.2$ and $\sigma = 5.0\ \sigma_{crit}$. Note the different scales for the vector lengths and pressure contours. The velocities are scaled on the lubrication scale. The insets show the details of the flow in the thin-film region.

time-scale implies that an increase in σ can be interpreted as an increase in the dimensional surface tension σ^*. This situation is characteristic of many pulmonary diseases and the results presented above indicate that an increase in σ via an increase in σ^* is strongly destabilising: it not only reduces the buckling pressure but also increases the growth rate of the instability. An alternative mechanism for an increase in $\sigma = \sigma^*/(R_0 K)$ is given by a structural weakening of the airway walls which occurs, e.g., in emphysema, and manifests itself in a reduction of the airway's bending stiffness K. A change to σ by this mechanism does not affect the fluid time-scale. Fig. 11 illustrates the system's evolution (for the same values of σ as before) on the lubrication theory time-scale t^*/T_L. The figure shows that an increase in σ at constant T_L leads to a partial stabilisation of the system: while the increase in σ still reduces the buckling pressure, the growth rates at a fixed value of the excess pressure are strongly reduced and it takes much longer for the catastrophic collapse and the associated airway closure to occur (if it does).

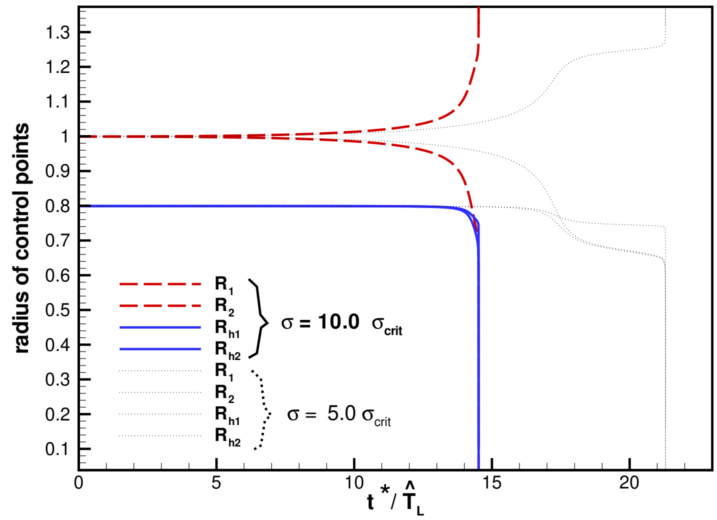

Figure 10: Comparison of the evolution of two liquid-lined rings for $\sigma = 17.28 = 10.0\ \sigma_{crit}$ and $\sigma = 5.0\ \sigma_{crit}$, respectively. $H_0 = 0.2$ in both cases.

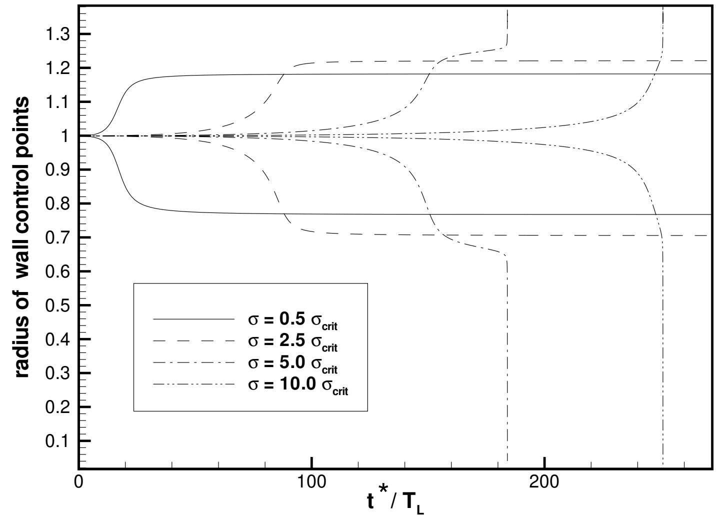

Figure 11: Evolution of liquid lined rings for various values of the non-dimensional surface tension σ versus time scaled on the lubrication theory time-scale. For clarity only the radii of the wall control points, R_1 and R_2 are shown. $H_0 = 0.2$ in all cases.

3.2.2 Inertial effects

The early stages of the ring's collapse are governed by the slow surface-tension-driven redistribution of fluid in the liquid lining and inertia is unlikely to be of great importance. However, wall and fluid inertia must be expected to play some role

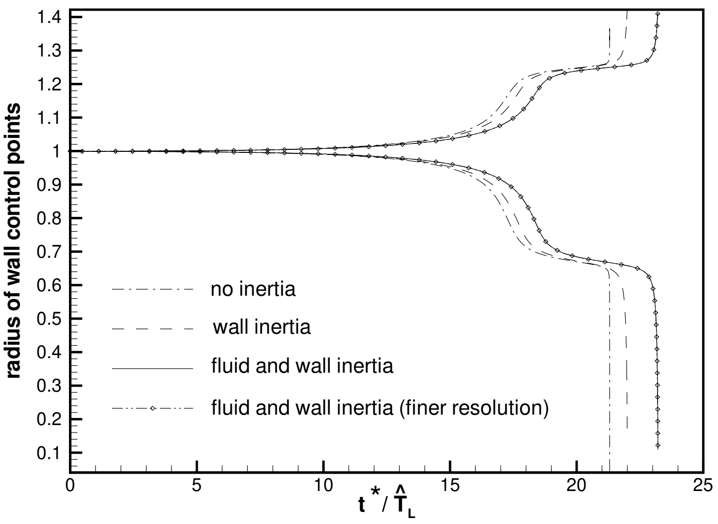

Figure 12: Effect of wall and fluid inertia on the evolution of a liquid-lined ring for $\sigma = 5.0\ \sigma_{crit}$ and $H_0 = 0.2$. For clarity, only the radii of the wall control points, R_1 and R_2, are shown. Note that the time-step is much smaller than the distance between the markers. $Re_L = 40,\ \Lambda_T = 8$.

during the rapid collapse of the air-liquid interface in the final stages of airway closure (if it occurs). To assess the significance of wall and fluid inertia, Fig. 12 compares the system's evolution (for $H_0 = 0.2$ and $\sigma = 5.0\ \sigma_{crit}$) with and without inertial effects. The relevant parameters, $Re_L = 40$ and $\Lambda_T = T_w/T_L = 8$, used in these computations are representative of those in the physiological problem (see section 4). Fig. 12 shows that inertia merely opposes any rapid changes while neither affecting the qualitative behaviour nor the final outcome of the instability. However, the addition of wall inertia has a secondary, more subtle effect which does not show up in Fig. 12 but makes accurate numerical simulations more computationally expensive. The inclusion of wall inertia enables the ring to carry out oscillations in two main modes: **(i)** low frequency bending oscillations whose time-scale T_w was used in the time-scale ratio λ_T and **(ii)** high frequency in-plane oscillations which correspond to the ring's axisymmetric 'breathing' mode. Both oscillations are excited by the fluid forcing but the amplitude of the high-frequency in-plane oscillations remains small because of the ring's large extensional stiffness. Nevertheless, these wall oscillations are transmitted into the fluid where they result in rapidly oscillating radial pressure gradients which are superimposed onto the slowly varying pressure field induced by the much slower bending deformations. To resolve these high-frequency oscillations, much smaller time-steps were required in the numerical integration.

3.2.3 Variation in the film thickness

We will now investigate the effect of variations in the initial film thickness H_0. Provided all other parameters remain unchanged, an increase to H_0 has two main effects: **(i)** the lubrication time-scale $T_L \sim H_0^{-3}$ is strongly reduced; **(ii)** the increase in the compressive load during buckling (caused by the reduction in luminal area and the associated increase in the curvature of the air-liquid interface) increases with H_0 (see Appendix C). The latter effect facilitates the occurrence of the catastrophic collapse since it is caused by the inability of the ring's bending moments to balance the increase in the compressive load during buckling. This is illustrated in Fig. 13 which shows the system's evolution for various values of the surface tension σ and for $H_0 = 0.3$ (corresponding to $\sigma_{crit} = 1.158$): for this larger film thickness, the catastrophic collapse can be seen to occur at much lower values of σ and in particular for $\sigma < \sigma_{crit}$. Computations at smaller values of H_0 confirm that a decrease in film thickness has the expected opposite effect, i.e. the growth rate of the instability is reduced and the catastrophic collapse occurs at larger values of σ; see Fig. 16 in the next section.

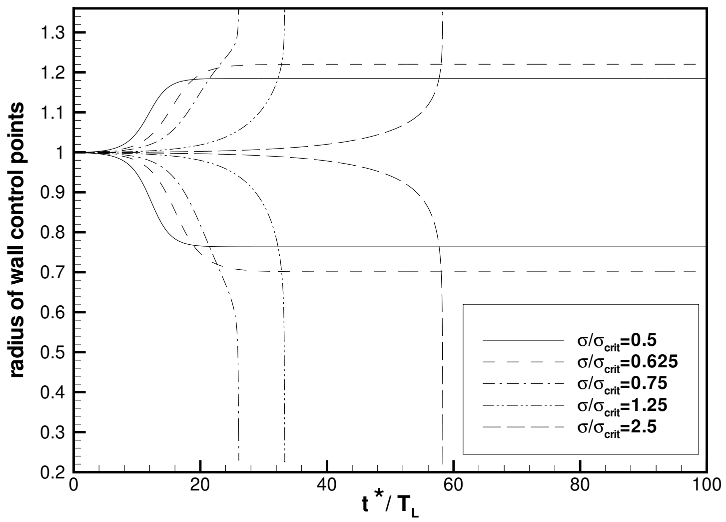

Figure 13: The evolution of a liquid-lined ring for $H_0 = 0.3$ and various values of σ/σ_{crit}, where $\sigma_{crit} = 1.158$. For clarity, only the radii of the wall control points, R_1 and R_2, are shown. Time is scaled on the lubrication theory time-scale.

3.3 Comparison with lubrication theory

Having established that the dynamics of the ring collapse are controlled by the surface-tension-driven redistribution of fluid in the liquid lining, we will now investigate if this behaviour can be captured by the lubrication theory model developed in section 2.2.2.

We will first assess the accuracy of the volume-conserving lubrication theory model in a model problem without fluid-structure interaction. For this purpose, we consider the flow in a fairly thick film (by the standards of lubrication theory) on a ring which buckles under the effect of an external pressure of $p_{ext} = 3.3$. Setting the non-dimensional surface tension to $\sigma = 0$ uncouples the ring's deformation from the fluid flow: the ring undergoes periodic large-displacement oscillations while the fluid redistributes itself passively on its surface. This is illustrated in Fig. 14 in which the solid and broken lines represent the control radii on the wall and the air-liquid interface, respectively. As the ring buckles, fluid drains out of the thin-film region

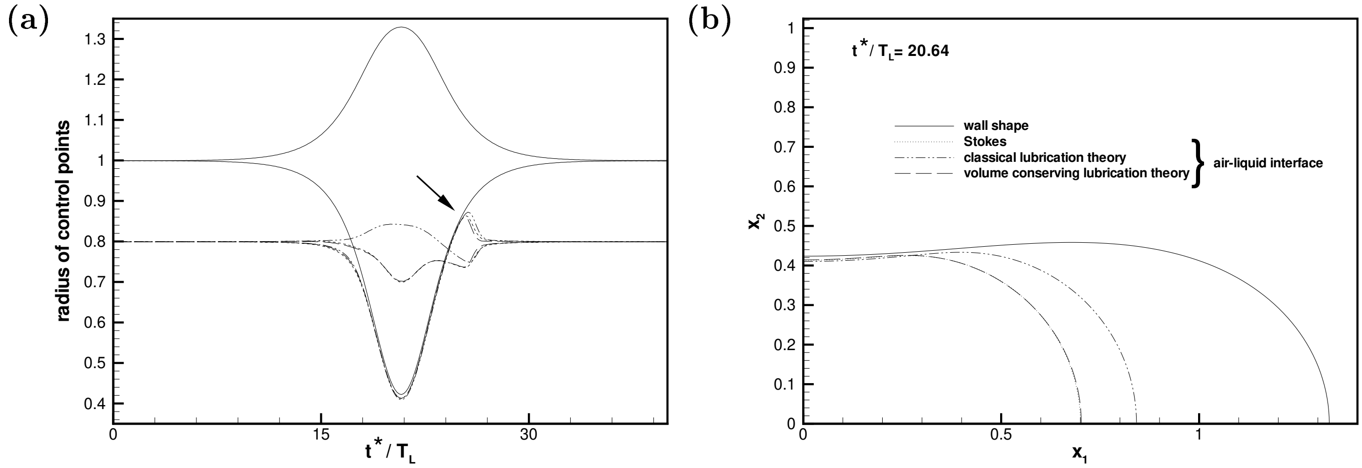

Figure 14: Comparison of Stokes flow and lubrication theory for the flow on a buckling ring without fluid-structure interaction. $H_0 = 0.2$, $\sigma = 0$, $\Lambda_T = 8$. (a) Plot of the control radii on the wall and the air-liquid interface. (b) Comparison of the wall and air-liquid interface positions at $t^*/T_L = 20.64$. The legend in (b) applies to both figures. Note that the Stokes flow solution is nearly indistinguishable from volume-conserving lubrication theory.

near the top of the ring ($R_2 - R_{h2} \to h_{2,min} \ll H_0 = 0.2$) as the surface-tension-induced pressure gradient drives fluid into the buckling lobe where the film thickens substantially ($R_1 - R_{h1} \to h_{1,max} \approx 0.65$ for Stokes flow). As the ring reopens, the flow reverses its direction and fluid moves back into the thin-film region. Because of the large flow resistance in the thin film, the initial phase of the film thickening takes place very slowly until, at $t^*/T_L \approx 25.4$ (marked by the arrow), the film has become thick enough to enable more rapid flows into this region. Following this, the fluid becomes more mobile, allowing the air-liquid interface to quickly return to an axisymmetric shape.

The dash-dotted and dashed lines in Fig. 14 represent the predictions for R_{h1} and R_{h2} from the 'classical' lubrication theory model (19) and from the volume conserving formulation (20)–(21), respectively. In both cases, the interface position was resolved by the method of spines and the exact expression for the interface curvature κ_h was used. The comparison with the results from the Stokes model (represented by the dotted line) shows that the 'classical' lubrication theory model strongly underestimates the film thickening in the lobe. In contrast, the volume conserving model is able reproduce the motion of the air-liquid interface extremely well, despite the fact that the film thickness can become rather large. This is confirmed by a representative plot of the wall and interface positions shown in Fig. 14(b).

We have performed a large number of such comparisons for different parameter values (film thicknesses, amplitudes of the wall displacement and time-scale ratios) and have found the agreement between Stokes flow and the volume-conserving lubrication theory model to be consistently good. We believe that this provides interesting insight into the fluid mechanics of this problem. The classical lubrication theory model (14) describes the surface-tension-driven flow into the buckling lobe and thus provides a partial explanation for the film thickening in this region. The discrepancy with the Stokes flow solution shows that the film thickening due to simple volume conservation is of equal importance in this problem. It is clear that if there is little or no surface-tension-driven flux along a liquid-lined substrate then an increase in the wall curvature alone must already lead to a significant thickening of the film. Classical lubrication theory fails to capture this effect.

We also note that the fluid velocities inside the buckled lobe can be of considerable magnitude and that the Stokes flow field differs noticeably from the simple unidirectional parabolic velocity profile assumed in lubrication theory (see Fig. 15c). The fact that the volume-conserving lubrication theory model is nevertheless capable of accurately capturing the interface motion indicates that the details of the flow field inside the lobe are of minor importance – they merely represent the two-dimensional flow field required to achieve overall volume conservation. The dynamics of the flow are controlled by the flow in the thin-film region in which the assumptions of lubrication theory remain valid throughout the system's evolution.

To assess the suitability of the volume-conserving lubrication theory model in the fully coupled fluid-structure interaction problem, we must also investigate the accuracy of the lubrication theory approximation (27) for the traction that the fluid exerts onto the wall. Figs. 15(a,b) show the Stokes velocity and pressure fields and the corresponding pressure distribution along the wall during the early stages of the ring's buckling. Note that lubrication theory assumes that **(i)** the wall-normal velocities are much smaller than the tangential velocities and **(ii)** the pressure remains uniform through the thickness of the liquid lining. Fig. 15(a) shows that these assumptions are violated most strongly near the lines of symmetry where the velocities tangential to the wall tend to zero, whereas the normal velocities (induced by the substrate motion) become relatively large. This generates a normal pressure gradient that is responsible for the noticeable curvature of the isobars in these regions and increases the stabilising effect of the fluid pressure on the wall deformation – the fluid pressure becomes more (less) compressive where the wall buckles outwards (inwards). This effect is not represented in the lubrication theory model, and thus its prediction for the pressure distribution underestimates the pressure variations along the wall as shown in Fig. 15(b).

During the later stages of the non-axisymmetric collapse, the fluid domain becomes clearly divided into two distinct regions, as shown in Fig. 15(c): the thin-film region in which lubrication theory is valid and the large region in the buckled lobe in which the pressure remains approximately uniform despite the significant flows induced by the volume-conserving redistribution of fluid. Fig. 15(d) shows that in this regime, lubrication theory provides an excellent prediction for the pressure distribution on the wall.

Figs. 16(a,b) illustrate the buckling of a ring which is lined with a film of initial thickness $H_0 = 0.1$ when the full fluid-structure interaction is taken into account

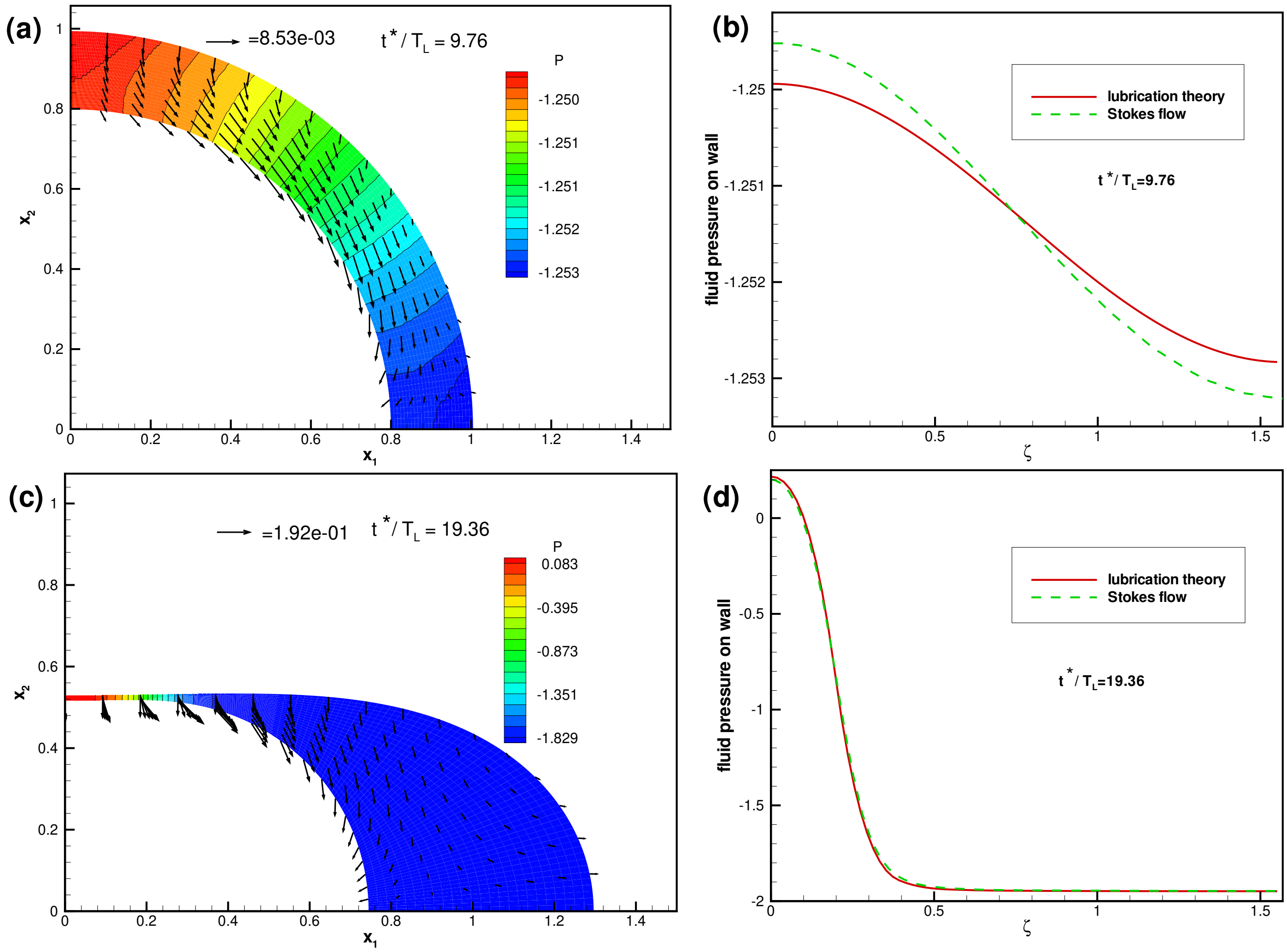

Figure 15: Flow on a buckling ring without fluid-structure interaction. $H_0 = 0.2$, $\sigma = 0$, $\Lambda_T = 8$. (a) and (c) show the Stokes velocity and pressure distribution in a slightly and strongly buckled ring; (b) and (d) show the corresponding Stokes and lubrication pressure distributions along the wall.

($\sigma = 10\ \sigma_{crit}$ and $\sigma = 100\ \sigma_{crit}$, respectively, where $\sigma_{crit} = 2.460$). The thick and thin lines represent the Stokes flow and lubrication theory results, respectively. Note that, as mentioned in section 3.2.3, at this smaller film thickness, the system can be subjected to much larger surface tensions, $\sigma/\sigma_{crit} \gg 1$, without undergoing a catastrophic collapse. Furthermore, the time-scale for the collapse can be seen to be significantly larger than for $H_0 = 0.2$. Since lubrication theory underestimates the stabilising effect of the fluid pressure distribution, it overestimates the initial growth rate of the non-axisymmetric instability. However, the lubrication theory model can be seen to capture the large-displacement behaviour extremely well since it provides a good approximation for the fluid traction in this regime.

Extensive further computations confirmed this behaviour for a wide range of parameters. The degree to which the lubrication theory model overestimates the

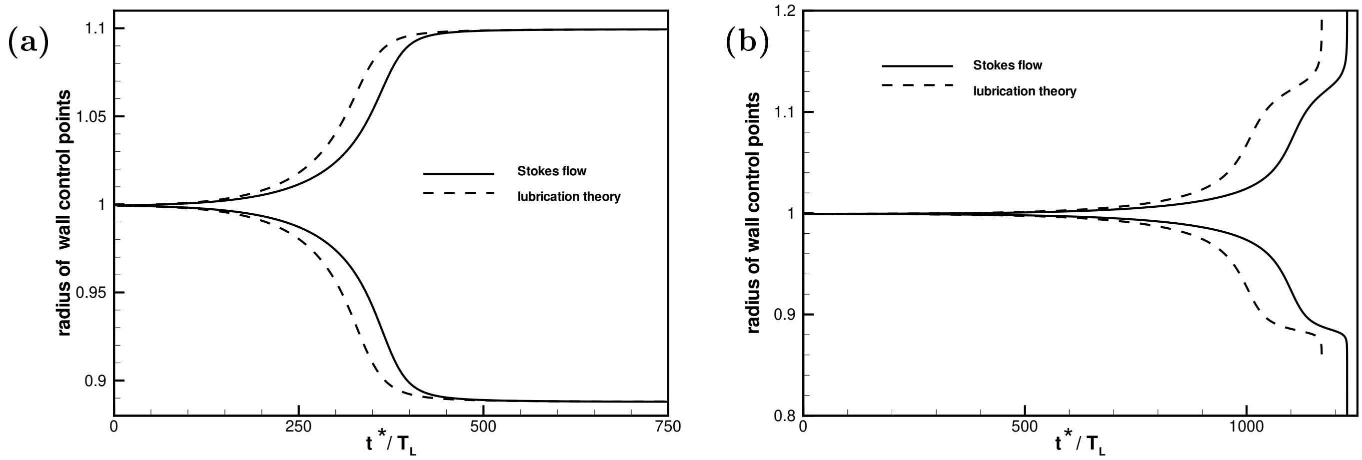

Figure 16: Comparison of Stokes flow and lubrication theory for the full fluid-structure interaction problem. $H_0 = 0.1$; no wall inertia. (a) $\sigma = 24.6 = 10\ \sigma_{crit}$ (b) $\sigma = 100\ \sigma_{crit}$. For clarity, only the radii of the wall control points R_1 and R_2 are shown. Time is scaled on the lubrication theory time-scale.

initial growth rate of the non-axisymmetric instability increases with the initial film thickness. However, even for thicker films, the large-displacement behaviour tends to be captured extremely well. Exceptions from this behaviour were only observed in cases where the ultimate catastrophic collapse was preceded by a period of slow change as in Fig. 8. In such cases, the small remaining differences between the Stokes and lubrication theory tractions were sufficient to significantly affect the time at which the ultimate collapse occurred. Note also that the computations based on the lubrication theory model could not be continued as far into the catastrophic collapse as those based on the solution of the (Navier-)Stokes equations. During the final, very rapid collapse, extremely small time-steps have to be used in the time integration of the discretised equations. During this phase of the computation, the condition number of the Jacobian matrix in the Newton iteration deteriorated significantly and caused severe convergence problems. These convergence problems were more pronounced in the lubrication theory computations and forced us to terminate the time integration at earlier times, as shown in Fig. 16(b).

4 Discussion

The numerical results presented in the previous sections show that, for sufficiently large surface tension, the dynamic post-buckling behaviour of liquid-lined circular rings is controlled by the dynamics of the surface-tension-driven redistribution of fluid in the liquid lining. This behaviour can be captured well by a volume-conserving lubrication theory model. An increase in surface tension was shown to be strongly destabilising; this is in agreement with Rosenzweig & Jensen's (2001) static analysis which identified σ_{crit} as the surface tension at which the static bifurcation changes its character from super- to sub-critical. This already suggests that an increase of σ beyond σ_{crit} will result in larger post-buckling displacements as the system has to evolve towards a 'more distant' non-axisymmetric equilibrium state. However, the time-dependent computations in the present study indicate that the system's dynamic post-buckling behaviour is more complicated than suggested by the static analysis. For instance, we have identified situations (mainly for relatively thick films) in which a catastrophic collapse can occur for $\sigma/\sigma_{crit} < 1$; also, some of the equilibrium states identified in Rosenzweig & Jensen (2001) require very long times to develop.

To assess the significance of the results for the physiological problem of airway closure we assume that the process takes place in the terminal bronchioli and use Halpern & Grotberg's (1992) estimates for the physical parameter values, namely $R_0 = 250\mu$m, $\sigma^* = 20$ dynes/cm, $\rho_w = \rho = 1000$ kg/m^3, $\mu = 10^{-3}$ kg/(m sec), $E = 6 \times 10^4$ dynes/cm^2, $\nu = 0.49$ and $h/R_0 = 1/10$. For an initial non-dimensional film thickness of $H_0 = 0.2$, as used in section 3, this corresponds to the non-dimensional parameters $\sigma = 120$, $Re_L = 40$, $\lambda_T = 774.9$ and $\Lambda_T = 6.20$. Of particular interest is the estimate for the non-dimensional surface tension σ since it is very much larger than the corresponding value of $\sigma_{crit} = 1.782$. Computations with the above parameter values yield a dimensional closure time (defined as the time between the onset of the non-axisymmetric instability and the occlusion of the airway) of $T_{clos} \approx 0.8$sec which is of the same order of magnitude as the period of a normal breathing cycle.

It is interesting to note that our investigation of the system's behaviour at constant excess pressure (which compensates for the initial destabilisation due to, e.g., an increase in surface tension) is directly applicable to the analysis of a common treatment of the neonatal Respiratory Distress Syndrome (nRDS). As mentioned in the introduction, nRDS is caused by the lack of surfactant in the lungs of prematurely born infants and makes their lungs strongly liable to collapse. In the context of the present work, the respiratory problems caused by the large surface tension can be attributed to both the reduction in buckling pressure and to the increased propensity of the airways to undergo a catastrophic collapse during which they become occluded. Mechanical ventilators used for the artificial respiration of infants suffering from nRDS tend to subject the infants' lungs to a positive base pressure which compensates for the additional surface-tension-induced compression and thus keeps their lungs distended. The artificial respiration often utilises a technique known as 'Positive End Expiratory Pressure (PEEP)' in which the gas exchange is performed by small-amplitude, high-frequency oscillations about this base state. This situation is very similar to the scenario considered in the present study: we compensated for the surface-tension-induced decrease of the buckling pressure by an appropriate reduction of the external pressure which kept the excess pressure $p_{exc} = p_{ext} - p_{buckl}$ constant.

It should be noted that physiological observations of airway closure show that the airways buckle with larger circumferential wave-numbers than considered in this study. This has motivated other investigators (e.g. Hill *et al.* 1997 and Rosenzweig & Jensen 2001) to consider buckling in higher wave-numbers despite the fact that $N = 2$ is the most unstable mode for this system. The increase in wavenumber in the physiological system is likely to be caused by finite length effects (shorter cylindrical tubes tend to buckle with higher circumferential wave-numbers; see Yamaki 1984), by the effect of the tethering provided by the surrounding lung tissue (Wang *et al.* 1983) and/or by the multilayer structure of the airway walls (Wiggs *et al.* 1997), all of which were neglected in the present study.

The film thicknesses used in the present study are larger than those typically encountered in an axially uniform liquid lining in the healthy lung (see, e.g., Bastacky *et al.* 1995). To some extent, the use of larger-than-average film thicknesses in our two-dimensional model is appropriate since in a three-dimensional airway, we expect buckling to be initiated only when and where the axisymmetric Rayleigh instability has led to a significant local increase in the film thickness. Nevertheless, we expect the results shown in the previous sections to be mainly applicable to situations in which diseases such as oedema have already led a noticeable thickening of the liquid lining.

The present study has neglected the role of surfactants, the presence of which is known to affect the dynamics of surface-tension-driven flows in the lung's liquid lining (see, e.g., Halpern & Grotberg 1993 or Yap & Gaver 1998). When the ring buckles, the flow into the buckling lobe advects surfactant into this region and thus reduces the local surface tension. This reduces the flow rate into the buckling lobe (and thus enhances the non-axisymmetry of the air-liquid interface) but it also reduces the stabilising effect of the non-uniform fluid pressure distribution. Since these two mechanisms have the opposite effect on the growth rate of the non-axisymmetric instability, it is not clear how the presence of surfactant will affect the dynamics of the non-axisymmetric airway collapse. However, the presence of surfactant will not change the static equilibrium positions towards which the system evolves. Therefore the final outcome of the non-axisymmetric instability is likely to be unaffected.

Finally, it should be stressed again that the analysis presented in this paper has neglected all three-dimensional effects and that we expect the three-dimensional system to be even more susceptible to airway closure than its two-dimensional counterpart. This implies that the paper's main conclusion, namely that airway closure can occur at fluid volumes which are too small to occlude an axisymmetric airway, also applies to the airways of the lung.

Acknowledgements

We are grateful to Dr. Andrew Hazel for many helpful discussions and would like to acknowledge financial support from the EPSRC for a PhD project studentship for JPW. We are also grateful to the anonymous referees whose comments led to a significant improvement of an earlier version of this paper.

Appendix A: The strain and bending measures

Given the parametrisation of the ring's deformed centreline in terms of the Lagrangian coordinate ζ, the strain and bending measures used in the principle of virtual displacements are defined as follows:

$$\gamma = \frac{1}{2}\left(\frac{\partial \mathbf{R}_w}{d\zeta}\cdot\frac{\partial \mathbf{R}_w}{d\zeta} - 1\right) \quad \text{and} \quad \kappa = -\left(1 - \mathbf{N}\cdot\frac{\partial^2 \mathbf{R}_w}{d\zeta^2}\right), \tag{33}$$

where

$$\mathbf{N} = \frac{\frac{d\mathbf{R}_w}{d\zeta} \times \mathbf{e}_3}{\left|\frac{d\mathbf{R}_w}{d\zeta} \times \mathbf{e}_3\right|} \tag{34}$$

is the inner unit normal on the deformed ring.

For small strain and moderate rotations, i.e. during the early stages of the rings collapse, the strain and bending measures can be approximated by Sanders's (1963) moderate rotation theory as

$$\gamma = \frac{1}{2}\left(v^2_{,\zeta} - v^1\right)^2 + v^1_{,\zeta} + v^2 \tag{35}$$

and

$$\kappa = v^1_{,\zeta} - v^2_{,\zeta\zeta}. \tag{36}$$

These expressions were used in the linear instability analysis.

Appendix B: Linear instability

Before buckling, the relation between the external pressure and the radial ring displacement V_0 is given by

$$p_{ext} = -\frac{12}{(h/R_0)^2}\, V_0 - \frac{\sigma}{1 + V_0 - H_1}, \tag{37}$$

where

$$H_1 = 1 + V_0 - \sqrt{(1+V_0)^2 + H_0(H_0 - 2)} = H_0 - \frac{H_0}{1 - H_0}\, V_0 + O(V_0^2) \tag{38}$$

is the pre-buckling film thickness which increases as the ring is compressed.

The growth rate ω of the normal mode perturbations (29) to the axisymmetric pre-buckling state is determined by the roots of the fifth order polynomial $\det\ \mathbf{M}(\omega) = 0$, where the coefficients of the matrix $\mathbf{M}$ are given by

$$\begin{aligned}
M_{11} &= \frac{1}{12}\left(\frac{h}{R_0}\right)^3 \omega^2 + N^2 + \frac{1}{12}\left(\frac{h}{R_0}\right)^2 N^2 \\
M_{12} &= -\frac{1}{12}\left(\frac{h}{R_0}\right)^2 \sigma H_1 i N \frac{N^2 - 1}{(1 + V_0 - H_1)^2} - \frac{1}{12} i N \left(12 + \left(\frac{h}{R_0}\right)^2 N^2\right) \\
M_{13} &= \frac{1}{12}\left(\frac{h}{R_0}\right)^2 \sigma H_1 i N \frac{N^2 - 1}{(1 + V_0 - H_1)^2} \\
M_{21} &= \frac{1}{12} i N \left(12 + 12 V_0 + \left(\frac{h}{R_0}\right)^2 N^2\right) \\
M_{22} &= 1 + V_0 N^2 + \frac{1}{12}\left(\frac{h}{R_0}\right)^3 \omega^2 + \frac{1}{12}\left(\frac{h}{R_0}\right)^2 N^4 + \frac{1}{12}\left(\frac{h}{R_0}\right)^2 \sigma \frac{N^2 - 1}{(1 + V_0 - H_1)^2} \\
M_{23} &= -\frac{1}{12}\left(\frac{h}{R_0}\right)^2 \sigma \frac{N^2 - 1}{(1 + V_0 - H_1)^2} \\
M_{31} &= 0 \\
M_{32} &= \frac{1}{3} H_1^3 N^2 \frac{N^2 - 1}{(1 + V_0 - H_1)^2} \\
M_{33} &= \frac{1}{\lambda_T}\omega - \frac{1}{3} H_1^3 N^2 \frac{N^2 - 1}{(1 + V_0 - H_1)^2}.
\end{aligned}$$

The system loses its stability when $\omega = 0$. This occurs at an axisymmetric pre-buckling displacement of

$$V_0^{(buckl)} = -\frac{1}{12}\left(\frac{h}{R_0}\right)^2 \left(N^2 - 1\right). \tag{39}$$

Since $h/R_0 \ll 1$, it follows that $|V_0^{(buckl)}| \ll 1$. Using this result in (37) shows that the buckling pressure is given by

$$p_{ext}^{(buckl)} = N^2 - 1 - \frac{\sigma}{(1 - H_0)} + O((h/R_0)^2) \tag{40}$$

Appendix C: The effect of an increase in H_0

To illustrate how an increase in the initial film thickness H_0 affects the increase in ring compression during buckling, we consider a slightly buckled ring whose initial non-dimensional cross sectional area $A_0 = \pi$ has been reduced to $A < A_0$. Mass conservation requires that the fluid always occupies the same cross sectional area $A_h = \pi H_0(2 - H_0)$. This leaves a luminal area of $A_L = A - A_h$ and we have $A_L \approx \pi/\kappa_h^2$ if the ring's deformation is small enough for an axisymmetric air-liquid interface (of curvature κ_h) to fit into the buckled ring without rupturing the liquid film. Combining these relations, we find that the pressure jump Δp over the air-liquid interface is given by

$$\Delta p = \sigma \kappa_h = \frac{\sigma}{\sqrt{A - \pi H_0(2 - H_0)}}. \tag{41}$$

This shows that $\partial \Delta p / \partial H_0 > 0$, implying that the additional compression of the ring for a given degree of collapse (specified by A) increases with H_0.

Appendix D: Comparison with Flaherty *et al.*'s (1972) wall model

The static analyses of Hill *et al.* (1997) and Rosenzweig & Jensen (2001) used Flaherty *et al.*'s (1972) inextensible Euler-Bernoulli model to describe the deformation of the airway wall. Fig. 17 compares the wall shapes predicted by Flaherty *et al.*'s (1972) model to those obtained from the Lagrangian wall model used in the present study. In both cases the ring deformation is induced by a spatially uniform external pressure. The predictions of the two models are in good agreement. Our decision to use the (arguably) more complex wall model described in section 2.1, was motivated by the fact that it is easier to extend it to three-dimensional geometries.

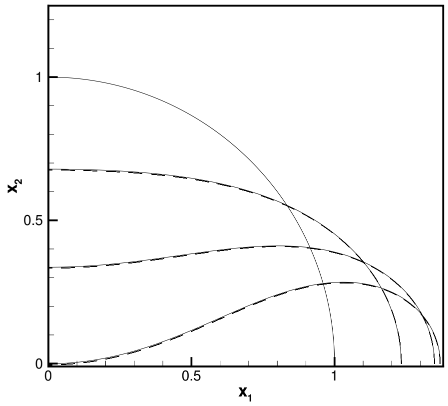

Figure 17: Deformation of a ring of wall thickness $h/R_0 = 1/20$ under constant external pressure. Solid lines: predictions from Flaherty *et al.*'s (1972) inextensible Euler-Bernoulli model; dashed lines: wall shapes from the Lagrangian model described in section 2.1. $p_{ext} = 3.0, 3.21, 3.87$ and 5.25.

References

Bastacky, J., Lee, C. Y. C., Goerke, J., Koushafar, H., Yager, D., Kenaga, I., Speed, T. P., Chen, Y. & Clements, J. A. 1995 Alveolar lining layer is thin and continuous – low-temperature scanning electron-microscopy of rat lung. *Journal of Applied Physiology* **79**, 1651–1628.

Bathe, K.-J. 1996 *Finite element procedures*, 2nd edn. Englewood Cliffs: Prentice-Hall.

Bogner, F. K., Fox, R. L. & Schmit, L. A. 1967 A cylindrical shell discrete element. *AIAA Journal* **5**, 645–750.

Demmel, J. W., Eisenstat, S. C., Gilbert, J. R., Li, X. S. & Liu, J. W. H. R. 1999 A supernodal approach to sparse partial pivoting. *SIAM Journal on Matrix Analysis and Applications* **20**, 720–755.

Everett, D. H. & Haynes, J. M. 1972 Model studies of capillary condensation. I. Cylindrical pore model with zero contact angle. *Journal of Colloid and Interface Science* **28**, 125–137.

Flaherty, J. E., Keller, J. B. & Rubinow, S. I. 1972 Post buckling behavior of elastic tubes and rings with opposite sides in contact. *SIAM Journal of Applied Mathematics* **23**, 446–455.

Forgacs, P. 1978 *Lung sounds*. London: Bailliere Tindall.

Gauglitz, P. A. & Radke, C. J. 1988 An extended evolution equation for liquid film breakup in cylindrical capillaries. *Chemical Engineering Science* **43**, 1457–1465.

Gaver, D. P., Halpern, D., Jensen, O. E. & Grotberg, J. B. 1996 The steady motion of a semi-infinite bubble through a flexible walled channel. *Journal of Fluid Mechanics* **319**, 25–56.

Halpern, D. & Grotberg, J. B. 1992 Fluid-elastic instabilities of liquid-lined flexible tubes. *Journal of Fluid Mechanics* **244**, 615–632.

Halpern, D. & Grotberg, J. B. 1993 Surfactant effects on fluid-elastic instabilities of liquid-lined elastic tubes: a model for airway closure. *ASME Journal of Biomechanical Engineering* **115**, 271–277.

Heil, M. 1999*a* Airway closure: Liquid bridges in strongly buckled elastic tubes. *ASME Journal of Biomechanical Engineering* **121**, 487–493.

Heil, M. 1999*b* Minimal liquid bridges in non-axisymmetrically buckled elastic tubes. *Journal of Fluid Mechanics* **380**, 309–337.

Heil, M. & Pedley, T. J. 1996 Large post-buckling deformations of cylindrical shells conveying viscous flow. *Journal of Fluids and Structures* **10**, 565–599.

Hill, M. J., Wilson, T. A. & Lambert, R. K. 1997 Effect of surface tension and intraluminal fluid on mechanics of small airways. *Journal of Applied Physiology* **82**, 233–239.

Howell, P. D., Waters, S. L. & Grotberg, J. B. 2000 The propagation of a liquid bolus along a liquid-lined flexible tube. *Journal of Fluid Mechanics* **406**, 309–335.

Hughes, J. M. B., Rosenzweig, D. Y. & Kivitz, P. B. 1970 Site of airway closure in excised dog lungs: histologic demonstration. *Journal of Applied Physiology* **29**, 340–344.

Jensen, O. E. 2000 Draining collars and lenses in liquid-lined vertical tubes. *Journal of Colloid and Interface Science* **221**, 38–49.

Johnson, M., Kamm, R. D., Ho, L. W., Shapiro, A. & Pedley, T. J. 1991 The non-linear growth of surface-tension-driven instabilities of a thin annular film. *Journal of Fluid Mechanics* **233**, 141–156.

Kistler, S. F. & Scriven, L. E. 1983 Coating flows. In *Computational Analysis of Polymer Processing* (ed. J. Pearson & S. Richardson). London: Applied Science Publishers.

Oron, A., Davis, S. H. & Bankoff, S. G. 1997 Long-scale evolution of thin liquid films. *Reviews of Modern Physics* **69**, 931–980.

Rayleigh, L. 1902 On the instability of cylindrical fluid surfaces. In *Scientific papers*, , vol. 3, pp. 594–996. Cambridge: Cambridge University Press.

Rosenzweig, J. & Jensen, O. E. 2001 Post-buckling instabilities of liquid-lined elastic tubes. *ASME Journal of Biomechanical Engineering* (submitted).

Ruschak, K. J. 1980 A method for incorporating free boundaries with surface tension in finite element fluid-flow simulators. *International Journal for Numerical Methods in Engineering* **15**, 639–648.

Sanders, J. L. 1963 Nonlinear theories for thin shells. *Quarterly Journal of Applied Mathematics* **21**, 21–36.

Schwartz, L. W. & Weidner, D. E. 1995 Modeling of coating flows on curved surfaces. *Journal of Engineering Mathematics* **29**, 91–103.

Soedel, W. 1993 *Vibrations of shells and plates*. New York: Marcel Dekker.

Taylor, C. & Hood, P. 1973 A numerical solution of the Navier-Stokes equations using the finite element technique. *Computers and Fluids* **1**, 73–100.

Wang, C. Y., Watson, L. T. & Kamat, M. P. 1983 Buckling, postbuckling, and the flow through a tethered elastic cylinder under external pressure. *ASME Journal of Applied Mechanics* **50**, 13–18.

Weidner, D. E., Schwartz, L. W. & Eres, M. H. 1997 Simulation of coating layer evolution and drop formation on horizontal cylinders. *Journal of Colloid and Interface Science* **187**, 243–258.

Wempner, G. A. 1981 *Mechanics of solids with applications to thin bodies*. Alphen aan den Rijn: Sijthoff & Noordhoff.

West, J. B. 1985 *Respiratory physiology – the essentials*. Baltimore: Williams & Wilkins.

Widdicombe, J. & Davies, A. 1991 *Respiratory physiology*, 2nd edn. London, Melbourne, Auckland: Edward Arnold.

Wiggs, B. R., Hrousis, C. A., Drazen, J. M. & Kamm, R. D. 1997 On the mechanism of mucosal folding in normal and asthmatic airways. *Journal of Applied Physiology* **83**, 1814–1821.

Yamaki, N. 1984 *Elastic stability of circular cylindrical shells*. Amsterdam: North-Holland.

Yap, D. Y. K. & Gaver, D. P. 1998 The influence of surfactant on two-phase flow in a flexible-walled channel under bulk equilibrium conditions. *Physics of Fluids* **10**, 1846–1863.